Ore Geology Reviews 75 (2016) 125–149

Contents lists available at ScienceDirect

Ore Geology Reviews

journal homepage: www.elsevier.com/locate/oregeorev

Geological, geochemical, and geochronological characteristics of Caledonian W–Sn mineralization in the Baiganhu orefield, southeastern Xinjiang, China

Jianhou Zhou [a], Chengyou Feng [a,*], Daxin Li [a], Guochen Li [b]

[a] MLR Key Laboratory of Metallogeny and Mineral Assessment, Institute of Mineral Resources, Chinese Academy of Geological Sciences, Beijing 100037, People's Republic of China
[b] Beijing Research Institute of Uranium Geology, Beijing 100029, People's Republic of China

ARTICLE INFO

Article history:
Received 13 July 2015
Received in revised form 12 December 2015
Accepted 12 December 2015
Available online 17 December 2015

Keywords:
Caledonian
W–Sn deposit
Greisen system
S-type granite
A-type granite
Post-orogenic setting

ABSTRACT

The newly discovered large-scale Baiganhu W–Sn orefield, consisting of the Kekekaerde, Baiganhu, Bashierxi, and Awaer deposits, is located in Ruoqiang County, southeastern Xinjiang, China. These deposits comprise mainly three types of W–Sn mineralization: early-stage skarn-type, middle-stage greisen-type, and late-stage quartz-vein-type. In this study, we classified seven major vertical zones on the basis of petrographic characteristics, roughly from the bottom of the parental granitic intrusions upward, as (A) fresh syenogranite, (B) argillic alteration, (C) muscovite-dominated greisenization, (D) tourmaline-dominated greisenization, (E) marginal facies (including K-feldspar pegmatite and fine-grained granite), (F) aplitic apophysis, and (G1) skarn or (G2) infilled silification zones. According to the alteration–mineralization assemblages and cross-cutting relationships, five stages of mineralization are recognized in the orefield (I, skarn stage; II, greisen stage; III, quartz vein stage; IV, argillic alteration stage; and V, supergene stage), and reverse alteration zonation in the altered intrusion is also observed.

The W–Sn deposits are spatially associated with syenogranite, which is part of the Caledonian Bashierxi magmatic series. Laser ablation–inductively coupled plasma–mass spectrometry (LA-ICP-MS) zircon U–Pb dating of the syenogranite yields a weighted mean $^{206}Pb/^{238}U$ age of 413.6 ± 2.4 Ma (MSWD = 0.36, n = 30). Hydrothermal muscovite from three samples associated with W–Sn mineralization yields plateau $^{40}Ar/^{39}Ar$ ages of 411.7 ± 2.6 Ma (MSWD = 0.21), 412.8 ± 2.4 Ma (MSWD = 0.22), and 413.8 ± 2.6 Ma (MSWD = 0.22), which is consistent with the zircon U–Pb age, thus indicating a temporal link between the emplacement of the syenogranite and the W–Sn mineralization. Our age data and previously published ages, along with geochemical data, for the granitoids in the Bashierxi magmatic series show a nearly contemporaneous evolution of A- and S-type granites, which were emplaced in a post-orogenic setting at ca. 432–413 Ma. As compared with the A-type granites, the syenogranites with S-type affinities probably resulted from a lower degree of partial melting of metagreywackes, which was more likely to be enriched in the ore-forming elements W and Sn, as well as volatiles such as B and H_2O. In addition, the syenogranites exhibit low oxidation states and underwent high degrees of factional crystallization, both of which favor post-magmatic W–Sn mineralization. We suggest that more attention should be given to buried syenogranites of S-type affinities during mineral exploration in this area, and that the proposed model of a vertical alteration zoning can act as a guide to the targeting of similar ore systems.

1. Introduction

China is the world's leading producer of W and Sn (Carlin, 2014; Shedd, 2015), most of which is mined in the Nanling region of southern China (Fig. 1a), where large-scale W–Sn deposits are associated mainly with granitic rocks of Yanshanian age (Mao et al., 2007; Feng et al., 2015 and references therein). Recently, ongoing exploration has revealed potentially medium- to large-scale W–polymetallic deposits related to Caledonian granitic rocks in northwest China (Zhou et al., 2015 and references therein), such as the Xiaoliugou W–Mo (Cu) orefield and the Xiliugou W–Mo (Cu) deposit in Gansu Province, and the Daheishan W deposit in Qinghai Province.

The Baiganhu W–Sn orefield, located ~250 km south of Ruoqiang County in the southeast Xinjiang Uygur Autonomous Region (Fig. 1b), is a newly discovered large-scale W–Sn orefield also associated with Caledonian granitic rocks (Li et al., 2012a; Wang et al., 2014b), consisting of the Kekekaerde, Baiganhu, Bashierxi, and Awaer deposits (Fig. 1c). Total indicated reserves for the first three deposits (as of 2013) are 174,913 t WO_3 and 79,091 t Sn, and the Baiganhu orefield and adjacent areas have been identified as a new W–Sn metallogenic province in China. Previous work on the Baiganhu orefield includes

* Corresponding author.
E-mail address: fengchy@cags.ac.cn (C. Feng).

http://dx.doi.org/10.1016/j.oregeorev.2015.12.009
0169-1368/

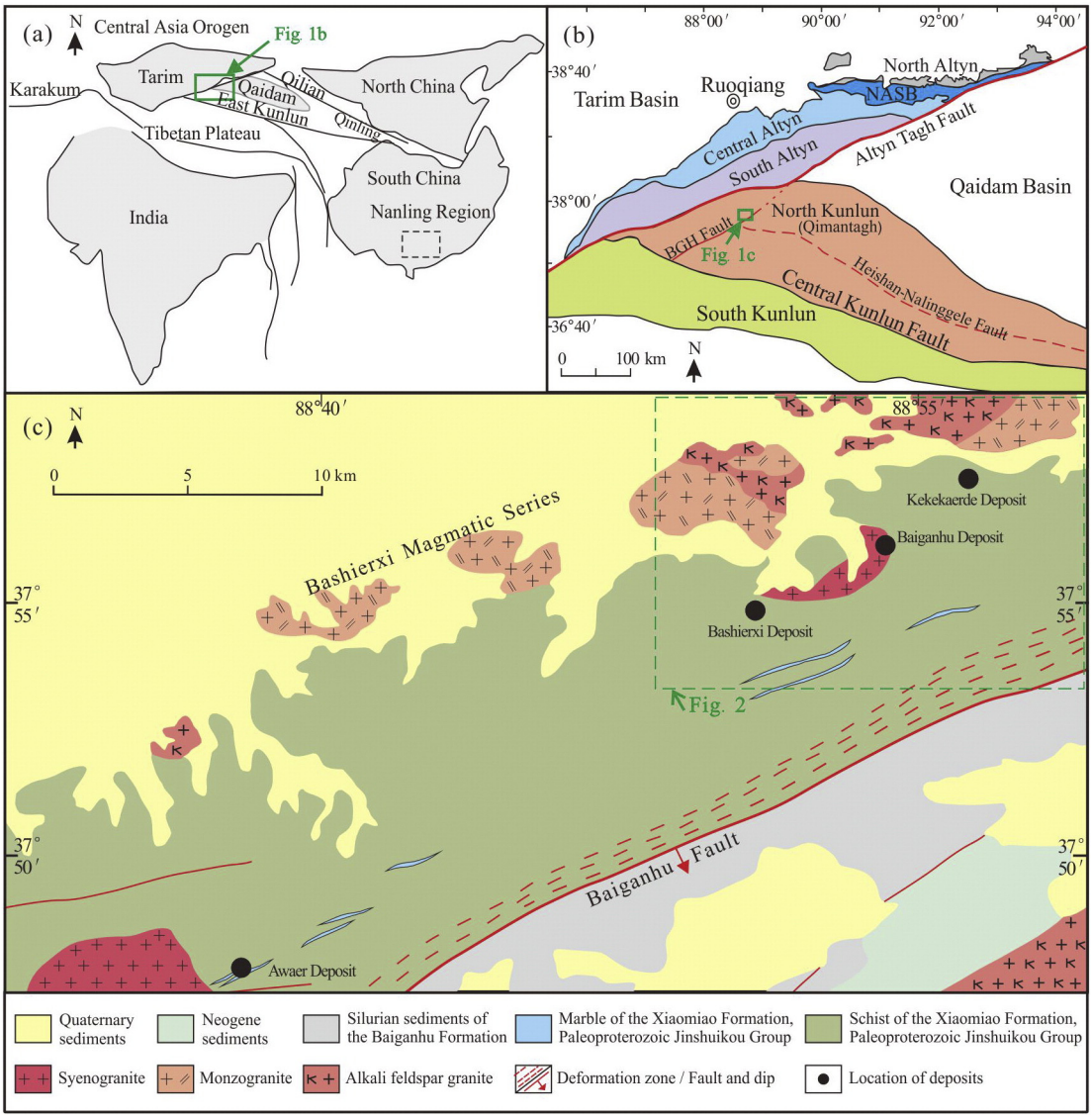

Fig. 1. (a) Location of the study area. (b) Distribution of the main geotectonic units in the Altyn Tagh and East Kunlun. After Wang et al. (2014a); BGH Fault = Baiganhu Fault; others see text for details). (c) Geological sketch map of the Baiganhu W–Sn orefield (after Jilin Geological Survey Institute, 2009).

studies on regional metallogenesis (Li et al., 2007), modeling of the genesis of the deposits (Liu et al., 2007), fluid inclusion microthermometry (Gao et al., 2011; Li et al., 2012b; Feng et al., 2013), and geochronological and geochemical studies on the Caledonian Bashierxi magmatic series (e.g., Bao et al., 2008; Gao et al., 2010; Gao and Li, 2011; Li et al., 2012a; Wang et al., 2014b). However, little is known about the alteration–mineralization features of these deposits, and no systematic research has been conducted on W–Sn mineralization of the Caledonian Bashierxi magmatic series.

In the present study, we conducted a detailed geological investigation of the mineralization and alteration of these deposits, and obtained hydrothermal muscovite ^{40}Ar–^{39}Ar ages of three samples associated with W–Sn mineralization. We also determined precise laser ablation-inductively coupled plasma-mass spectrometry (LA-ICP-MS) zircon U–Pb ages for the parental syenogranite, together with petrographic, mineralogical, whole-rock geochemical, and Hf isotopic data. These data were examined in combination with previously published data on the Bashierxi magmatic series, so as to better understand the genesis of the deposits and their relationship to mineralization, and to investigate the tectonic setting in which the W–Sn deposits formed.

2. Geological setting

Tectonically, the Baiganhu W–Sn orefield is situated at the junction of the Arkyn Tagh terrane and the East Kunlun terrane (Fig. 1a). The orefield is bounded by the Arkyn Tagh Fault to the north (located ~20 km from the orefield) and by the Baiganhu Fault to the east (located ~2–3 km from the orefield) (Fig. 1b). The Altyn Tagh terrane is subdivided into four units based on stratigraphic, metamorphic, structural, and age relationships; from north to south; these are the Archean North Altyn Tagh terrane (North Altyn), the early Paleozoic North Altyn Tagh subduction–collision belt (NASB), the Central Altyn massif (Central Altyn), and the South Altyn Tagh subduction–collision belt (South Altyn) (Fig. 1b; Liu et al., 2009). The East Kunlun terrane, which encompasses both the North Kunlun and South Kunlun terranes, is separated by the NW-trending Central Kunlun Fault, which is a major suture zone (Fig. 1b; Xu et al., 2006). The western part of the North Kunlun terrane (bordering the South Altyn region) is known as the Qimantagh area.

Rocks that outcrop in the Baiganhu orefield consist mainly of the Xiaomiao Formation of the Paleoproterozoic Jinshuikou Group and the

Baiganhu Formation of the Silurian Qimantage Group. These two formations are separated by the NE-trending Baiganhu Fault (Fig. 1c). The Xiaomiao Formation, which crops out to the north of the Baiganhu Fault, consists mainly of low-grade metamorphosed sericite–quartz schist and marble with minor plagiogneiss, and thus the protoliths were either siliciclastic or carbonate sedimentary rocks with minor volcanic rocks; this formation is the major host rock of the W–Sn deposits. The Baiganhu Formation, which crops out to the south of the Baiganhu Fault, consists mainly of low-grade metamorphosed graptolite-bearing shale facies. The major constituents of this formation are slate and phyllite derived from mudstone and siltstone.

The NE-trending distribution of intrusions and mineral deposits in the orefield are controlled mainly by the NE-trending Baiganhu Fault (Figs. 1c, 2). To the south of these deposits, a 2.5–5.0-km-wide deformation zone is developed along the Baiganhu Fault. The fault strikes at ~060° and extends for ~230 km. It is obliquely crossed at its northeastern end by the Altyn Tagh Fault. Thus, it has been postulated that the Baiganhu Fault is a subfault of the Altyn Tagh Fault (Li et al., 2013). According to a 1:100,000 stream sediment survey conducted in the region (Li et al., 2007), mineralization assemblages with strong elemental anomalies occur along both sides of the Baiganhu Fault, indicating that the fault has exerted strong controls on W, Sn, Au, and Cu mineralization in the region.

The *Caledonian Bashierxi magmatic series*, which is spatially associated with the W–Sn deposits, was intruded into the Xiaomiao Formation as stocks, batholiths, or apophyses (alternatively referred to as dikes). The series consists of 20 major intrusions, which crop out over a total exposed surface area of ~275.5 km^2 (Li et al., 2013). Lithologically, the series consists mainly of monzogranite, alkali feldspar granite, and syenogranite (Fig. 3).

In the northern part of the orefield, the Bashierxi magmatic series occurs mainly as stocks or batholiths of monzogranite or alkali feldspar granite (Figs. 1c, 2). Two types of enclaves are common in both of these granitoids: (1) wall-rock enclaves of schistose, metasandstone, or gneissic components, and (2) mafic microgranular enclaves (MMEs) of mainly dioritic and smaller amounts of mafic components (Li et al., 2013). The monzogranites and alkali feldspar granites, which exhibit subhedral to anhedral coarse-grained textures, are generally quite fresh. The *monzogranites* (Fig. 3a,b) are light red in color, and the major rock-forming minerals are K-feldspar (>10 mm, 35% — 40% by volume; note that all percentage values below are by volume), plagioclase (25% — 30%), quartz (25% — 30%), biotite (5% — 10%), and hornblende (±5%). The *alkali feldspar granites* (Fig. 3c,d) are blood red in color, and consist mainly of K-feldspar (>10 mm, 60%–65%), quartz (25% — 30%), biotite (5% — 10%), and plagioclase (<5%). Accessory minerals in both rocks include titanite, apatite, and zircon (inherited zircon is hardly present, as determined by cathodoluminescence (CL) images; Li et al., 2012a). Based on petrographic observations, the mafic minerals (hornblende and/or biotite) of both rocks formed later than or were contemporaneously with quartz or feldspar of magmatic origin (Fig. 3b,d). Zircon U–Pb dating of monzogranites and alkali feldspar granites by LA-ICP-MS and secondary ion mass spectrometry (SIMS)

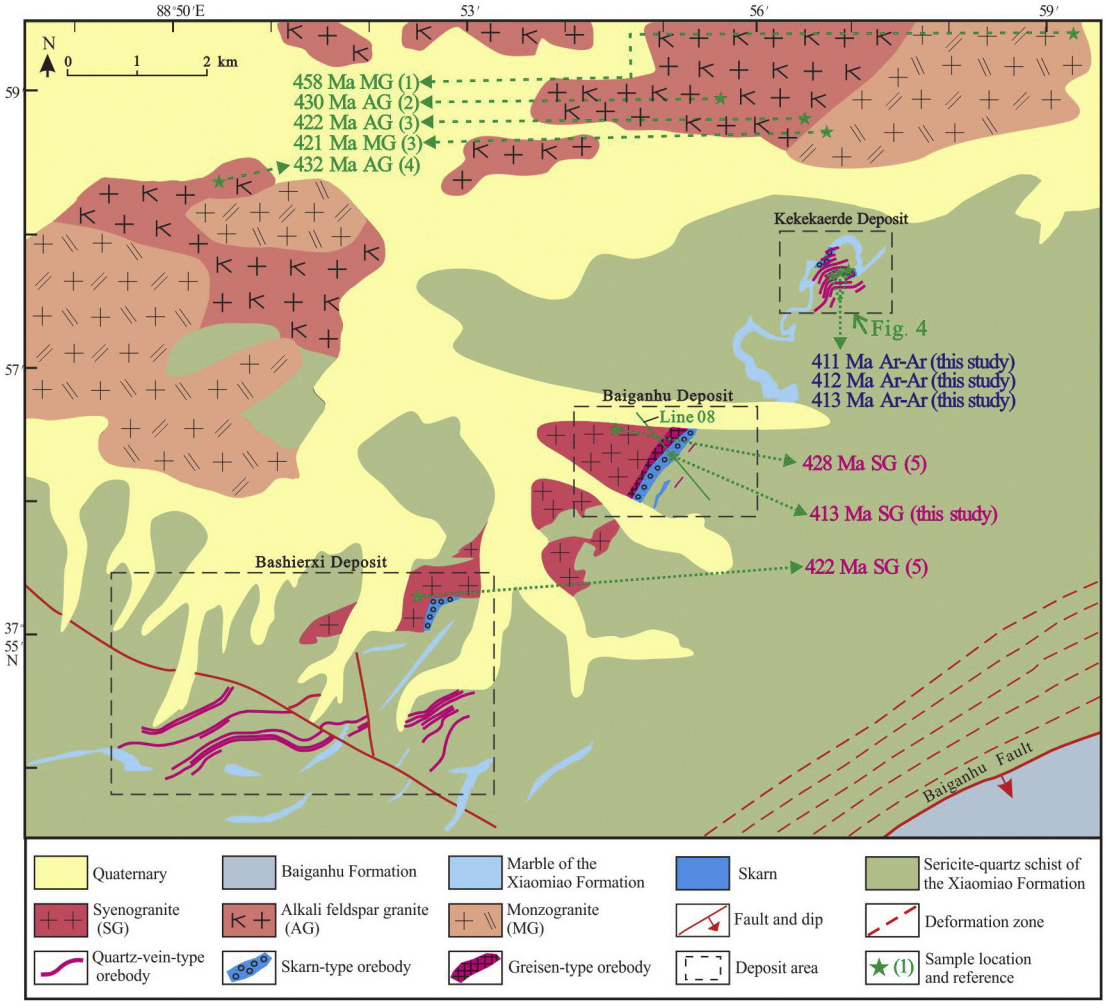

Fig. 2. Schematic geological map of the northeastern Baiganhu W–Sn orefield. After Jilin Geological Survey Institute (2009). References: (1) — Gao et al., 2010; (2) — Gao and Li, 2011; (3) — Li et al., 2012a; (4) — Bao et al., 2008; and (5) — Wang et al., 2014b.

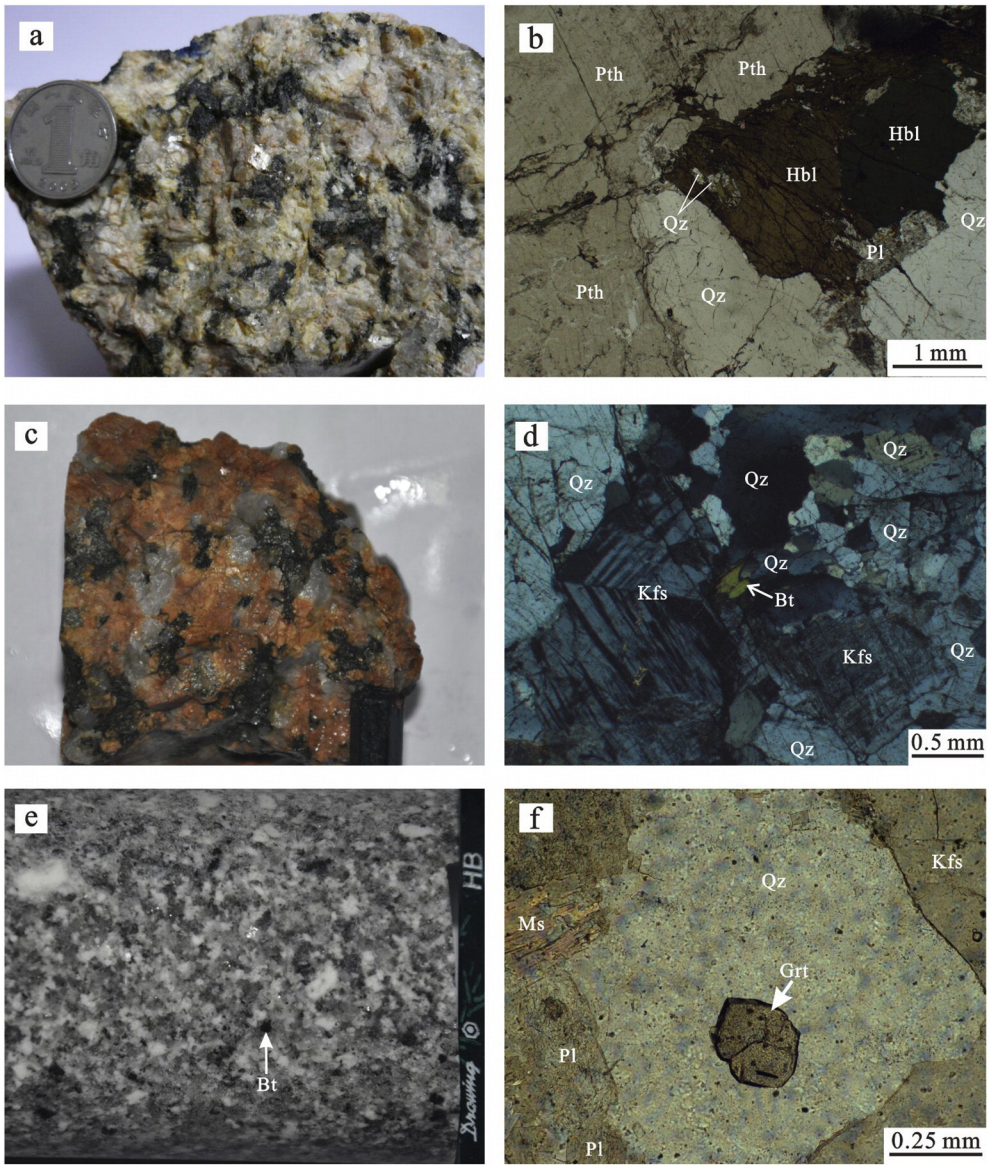

Fig. 3. Photographs and photomicrographs of the granitoids of the Bashierxi magmatic series (b and f, plane polarized light; d, cross polarized light). (a) and (b) Monzogranite, hornblendes penetrate in the interstices between felsic minerals or enclave the quartz. (c) and (d) Alkali feldspar granite, biotites occur as anhedral or subeuhedral crystals in the interstices between felsic minerals. (e) and (f) Syenogranite, biotites occur as euhedral or subeuhedral crystals and the accessory minerals contain garnet. The size of the coin in (a) is 19 mm, the width of the pencil in (b) and (c) is 7 mm. Mineral abbreviations (also for Figs. 6, 7, 8): albite (Ab), actinolite (Act), biotite (Bt), cassiterite (Cst), chlorite (Chl), diopside (Di), garnet (Grt), hornblende (Hbl), K-feldspar (Kfs), muscovite (Ms), plagioclase (Pl), perthite (Pth), pyrite (Py), quartz (Qz), scheelite (Sch), tourmaline (Tou), tremolite (Tr), and wolframite (Wol).

has yielded crystallization ages of ca. 432–421 Ma (Fig. 2; Bao et al., 2008; Gao and Li, 2011; Li et al., 2012a).

In the Baiganhu and Bashierxi deposits, the Bashierxi magmatic series intrudes the Xiaomiao Formation as stocks, with an exposed surface area of ~2.5 km^2 (Fig. 2). In the contact zone between the pluton and the Xiaomiao Formation, strong greisenization, skarnization, and silicification result in greisen-type scheelite ± wolframite mineralization in the inner contact zone, skarn-type scheelite mineralization in syncontact zones, and quartz-vein-type wolframite ± cassiterite ± scheelite mineralization in the outer contact zone (Fig. 2). A detailed petrographic study of fresh samples from this stock, obtained far from the contact zone, shows characteristics of syenogranite (Fig. 3e,f). These *syenogranites* are gray to white in color, and possess mainly a subhedral medium granular texture that locally grades into a porphyritic texture at the base of the pluton. The main minerals in the fresh syenogranite samples are K-feldspar (2–5 mm, 40%–45%), quartz (2–5 mm, 30%–35%), plagioclase (2–5 mm, 20%–25%), and minor biotite (1–3 mm, ±5%) and magmatic muscovite (1–3 mm, ±5%), with accessory minerals such as garnet (Fig. 3f), zircon, apatite, and ilmenite inclusions in the quartz, feldspar, and biotite crystals. The LA-ICP-MS zircon U–Pb dating of the syenogranite exposed in the Baiganhu and Bashierxi deposits yields a crystallization age of ~428–422 Ma (Fig. 2; Wang et al., 2014b).

In the Kekekaerde and Awaer deposits (Figs. 1c, 2), the Bashierxi magmatic series occurs mainly as buried plutons with strong greisenization (Figs. 4, 5). At present exploration levels, the plutons are also considered to be of syenogranitic composition; while no fresh samples of the parental intrusions have been obtained from either deposit, both intrusions exhibit magmatic garnets similar to those in the Baiganhu and Bashierxi deposits, and the alteration and related W–Sn mineralization slightly distinguish the Kekekaerde and Awaer deposits from the Baiganhu and Bashierxi deposits.

In all four deposits (Kekekaerde, Awaer, Baiganhu, and Bashierxi), some apophyses (or dikes), with widths of 0.02–2 m and occurring at distances of 50–100 m from the concealed syenogranite plutons, can be observed at the surface (Figs. 4–6). Potassic-feldspar pegmatites, which occur mainly as individual 0.1- to 2-m-thick layers with several

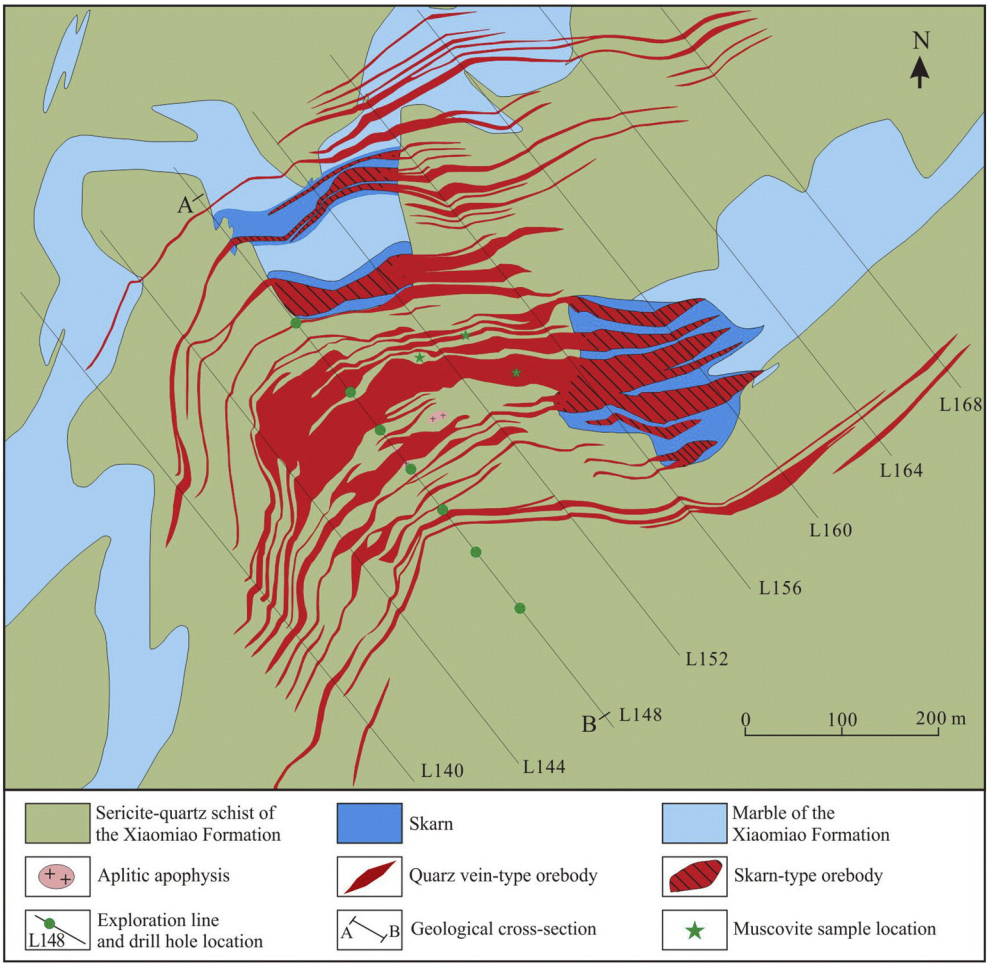

Fig. 4. Schematic geological map of the Kekekaerde W–Sn deposit (after Jilin Geological Survey Institute, 2009; see Fig. 5 for cross-section A–B (along Line 148).

repetitions and with total thicknesses of 5–20 m, are also present within the boundary zone between the syenogranite cupolas and the metasediments. In the deposits, the shapes of the mineralized syenogranite are similar to the 'frustum of a cone', in which upper and lower diameters are ~100 m and 450 m, respectively, and heights are ~250 m.

3. Geology of ore deposits

3.1. Ore zones and orebody type

This study focused mainly on deposits in the northeast part of the Baiganhu orefield (Fig. 1), as the deposits in this area are large and are undergoing intensive exploration. As of 2013, a total of 76 discrete mineral occurrences had been discovered in the northeast region, which, on the basis of geographical affinities, can be grouped into three different deposits (from NE to SW, the Kekekaerde, Baiganhu, and Bashierxi deposits) (Fig. 2). Three types of economic W–Sn orebodies have been identified in the deposits, based on styles of alteration and mineralization: quartz-vein-type, greisen-type, and skarn-type mineralization, comprising ~50%, ~25%, and ~25%, respectively, of the total occurrences in the orefield. Each of the three deposits contains all three types of mineralization, although the proportions of each type vary: skarn-type mineralization dominates in the Baiganhu deposit (Fig. 7); quartz-vein-type mineralization dominates in the Bashierxi deposit (Fig. 2); and greisen-type mineralization dominates in the Kekekaerde deposit, although quartz-vein- and skarn-type mineralization is also abundant (Figs. 4, 5).

Skarn-type orebodies are localized in the contact zone between syenogranite and marble wallrock enveloping the intrusion. The host rocks, skarn, and skarnized marble are interbedded with quartz–sericite schists of the Xiaomiao Formation. The orebodies are mostly bed-like or lenticular in shape, and occur at elevations of 4150–4300 m above sea level. They exhibit a generally NE strike, and dip to SE. The skarn-type orebodies of the Kekekaerde deposit strike at 050°–060°, and show variable dips of 20°–60° to the southeast. The thicknesses of the orebodies vary from several to tens of meters (Figs. 4, 5). In the Baiganhu deposit, the length of the skarn-type orebodies is 120–1300 m; they are 5–60 m thick, strike at 40°–87°, and dip 70°–80° to the southeast (Figs. 2, 7). In the Bashierxi deposit, skarn-type orebodies locallly occur as discontinuous small-scale lenticular bodies (Fig. 2). The host lithologies are mainly tremolite–diopside skarn and actinolite–diopside skarn, and to a lesser extent skarnized marble.

The main economic ore mineral in the Baiganhu deposit is scheelite (Figs. 6a′, 7d″). The scheelite generally occurs as fine grains disseminated in the skarn, or as coarse tabular crystals accompanying actinolite, tremolite, diopside, and quartz; the grain size is generally 0.2–5.0 mm (maximum, 15 mm). The gangue minerals consist mainly of quartz, diopside, actinolite, tremolite (Fig. 7d,d′), and calcite, as well as minor garnet, phlogopite, zoisite, and clinozoisite. In the Baiganhu deposit, the WO_3 content of the skarn-type orebodies is in the range of 0.15%–1.07% by weight (average, 0.37% by weight) (WO_3 contents given below are also expressed by weight).

Greisen-type orebodies are developed mainly in the endocontact zone, especially within the upper part of the concealed intrusion cupola, and within the greisenized aplitic apophysis that emanates from the

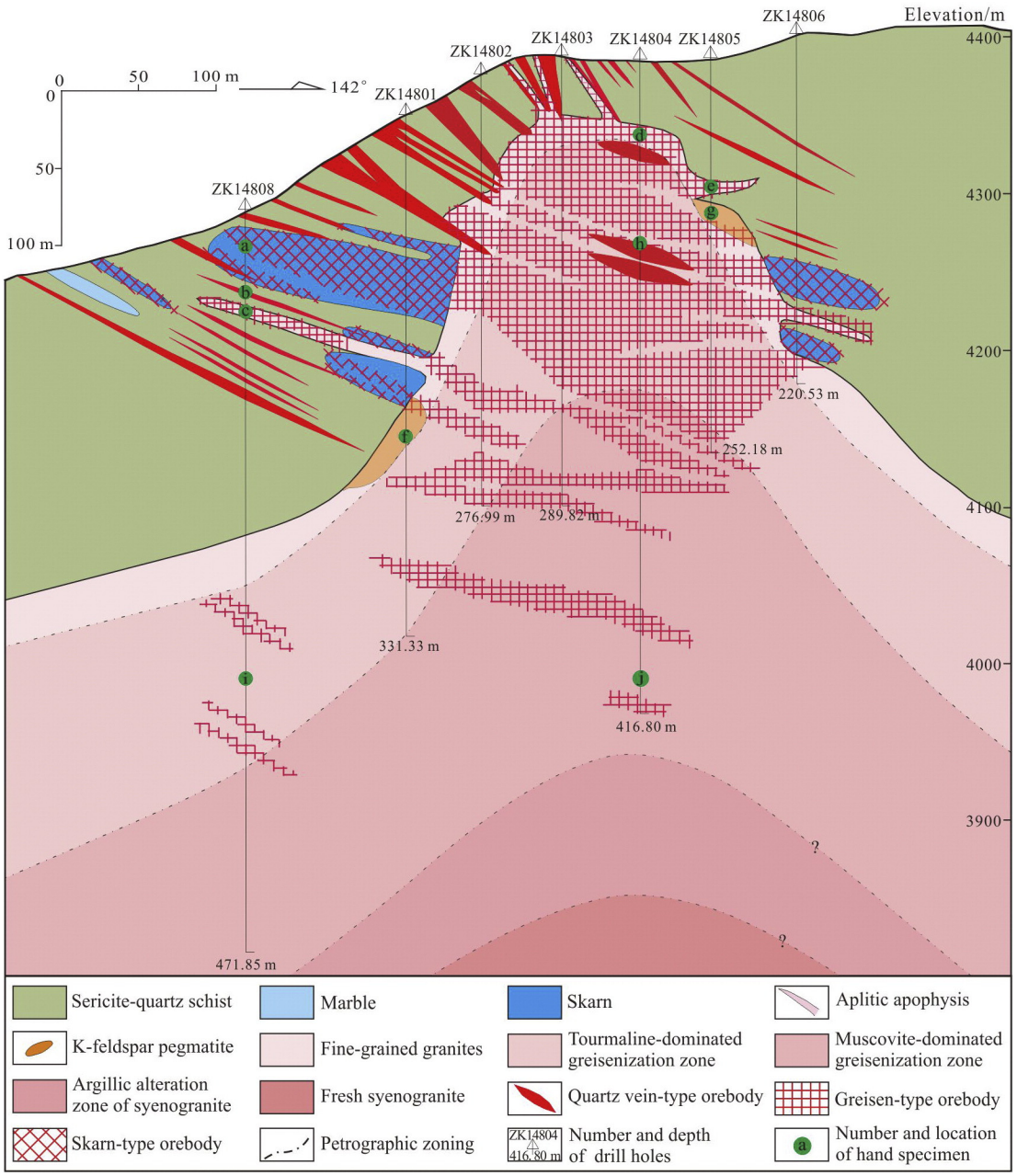

Fig. 5. Geological cross-section (A–B) through the Kekekaerde W–Sn deposit (after Jilin Geological Survey Institute, 2009; see text for detail petrographic zones).

cupola (Fig. 5). No apparent boundary is present between greisen-type orebodies and the greisen phase of alteration; hence, the orebodies are usually defined geochemically, as WO_3 contents of ≥0.15%. The greisen-type orebodies are mostly bed-like or lenticular in shape, and to a lesser extent occur as vein-type orebodies in the metasedimentary wallrock above the cupola (Fig. 5). The host rocks are mostly pervasively greisenized syenogranites or greisen. The ores are predominantly disseminated, with mainly blastogranitic or granolepidoblastic textures (Fig. 7b,f). Ore minerals are predominantly scheelite with smaller amounts of wolframite, cassiterite, pyrite, arsenopyrite, pyrrhotite, molybdenite, and sphalerite. Gangue minerals include quartz, tourmaline (abundant), K-feldspar, plagioclase, muscovite, and rare fluorite and topaz.

Typical greisen-type orebodies occur in the Kekekaerde deposit (Figs. 5, 6). These orebodies occur as bed-like, sheeted, or lenticular in the upper part of the cupola of buried intrusions, at elevations of 4000–4350 m (Fig. 5). They occur as discrete orebodies extending for 150–250 m with thicknesses of 1.25–43.07 m, strikes of 030°–060°, and dips of 10°–48° to the southeast. The WO_3 contents of these orebodies are 0.15%–0.42% (average, 0.24%). More detailed descriptions of the zoning of the greisen phase of alteration and its relationship to W–Sn mineralization are presented in the next section.

Two types of quartz-vein-type mineralization are recognized. The early type is represented by wolframite ± cassiterite ± scheelite-bearing quartz veins trending NEE to NE (Figs. 2, 4). The later type is represented by some NE-trending quartz veins that contain pyrite ± chalcopyrite ± sphalerite ± rare molybdenite. However, no economic Cu/Zn/Mo orebodies have yet been confirmed; thus, the focus of the following discussion is on W–Sn-bearing quartz-vein-type orebodies (simplified as 'quartz-vein-type orebodies').

Quartz-vein-type orebodies are common in the exocontact zone, especially in fractures and fissures in metasediments (Figs. 2, 4, 7), and to a lesser extent in the endogranite (Fig. 5). The shapes and occurrences of the orebodies show considerable variations, with quartz

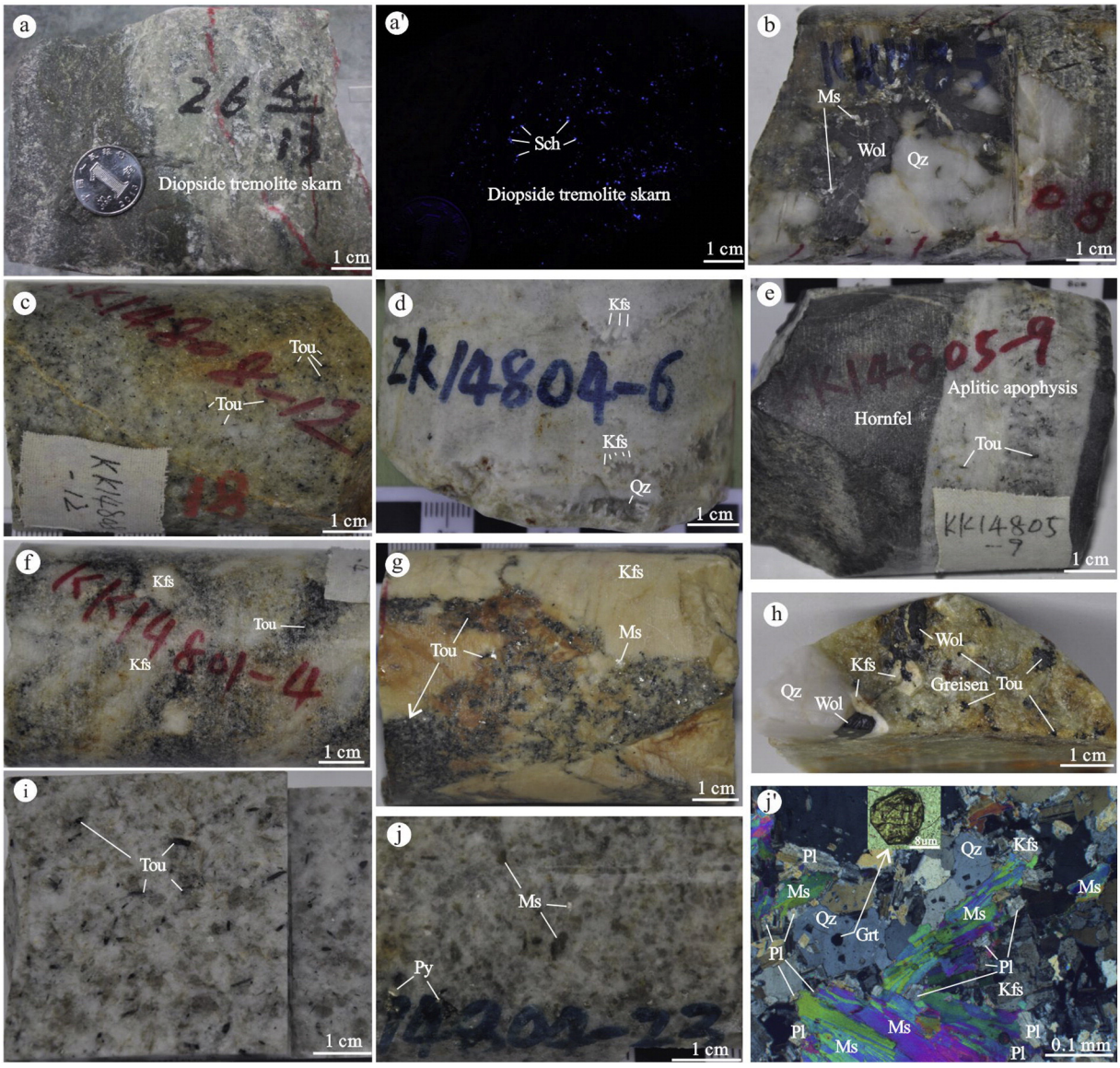

Fig. 6. Photographs showing alteration and mineralization in the Kekekaerde W–Sn deposit (see Fig. 5 for locations of hand specimens. (a′) identical to (a) but under ultraviolet light; (j′) identical to (j) but under the microscope.) (a) and (a′) Diopside–tremolite skarn with disseminated scheelite. (b) Wolframite-bearing quartz vein associated with hydrothermal muscovite. (c) and (e) Tourmaline-bearing aplitic apophyses. (d) Fine-grained granites with miarolitic cavities. (f) and (g) K-feldspar pegmatites occurring in the marginal contact zone. (h) Wolframite-bearing quartz vein and tourmaline-bearing greisen within the upper part of the intrusion. (i) Tourmaline-dominated greisenization zone. (j) and (j′) Muscovite-dominated greisenization zone, where magmatic garnet is preserved. Mineral abbreviations are as in Fig. 3.

veins bifurcating or recombining, expanding or narrowing. The veins are controlled by fractures and fissures, probably resulting from region tectonic activity and enhanced by intruding granitoids. In the Kekekaerde deposit, the orebodies occur mainly above the cupola in the exocontact zone of the quartz–sericite schists, generally at intervals of 20–50 m (Figs. 4, 5). The orebodies extend for 500–800 m, strike at 030°–050°, and dip at 12°–60° to the southeast. Some W–Sn-bearing quartz veins occur within the upper parts of the concealed greisenized cupola (Fig. 5), where infilled spaces are interpreted to be the result of fracturing and space-releasing conditions caused by solidification of the cooling syenogranitic magma. The Bashierxi deposit contains 45 quartz-vein-type orebodies (defined by cutoff grades of 0.15% WO_3 and 0.10% Sn). These orebodies occur mainly in the exocontact zone; they are 200–720 m in length and 1.15–22.5 m in width, strike at 060°–090°, and dip to SE (Fig. 2).

This type of orebody contains mostly the ore minerals wolframite and cassiterite, as well as minor scheelite and small amounts of chalcopyrite, pyrite, and rare molybdenite. The gangue minerals include quartz, muscovite, tourmaline, K-feldspar, fluorite, and calcite. Wolframite shows euhedral or hypidiomorphic tabular textures and occurs as discrete grains, mainly 2–50 mm in size, and generally as comb aggregates growing vertically along the walls of quartz veins or as intergrowths with muscovite in quartz veins (Figs. 6b, 8b,c). In the Kekekaerde deposit, wolframite locally develops as megacrystal aggregates, with sizes of up to 10 cm. Cassiterite occurs mainly as euhedral or hypidiomorphic tetragonal bipyramids, with individual grains generally 0.5–5 mm in size (single grains can be up to 5 cm) and to a lesser extent as anhedral grains; both euhedral and anhedral grains are generally associated with wolframite. Polysynthetic twins are common in the cassiterite. Scheelite occurs mainly as disseminated grains 0.1–3.0 mm in size, locally up to 1 cm. Some scheelite also occurs as veinlets or irregular fine grains replacing wolframite in quartz veins. Small amounts of sulfides, such as pyrite and chalcopyrite, are disseminated in the later quartz veins. The ore grade of the quartz-vein-type orebodies in the orefield is relatively high, and varies in the range of 0.15%–1.77% for WO_3 (average, 0.30%) and 0.10%–0.56% for Sn (average, 0.30%).

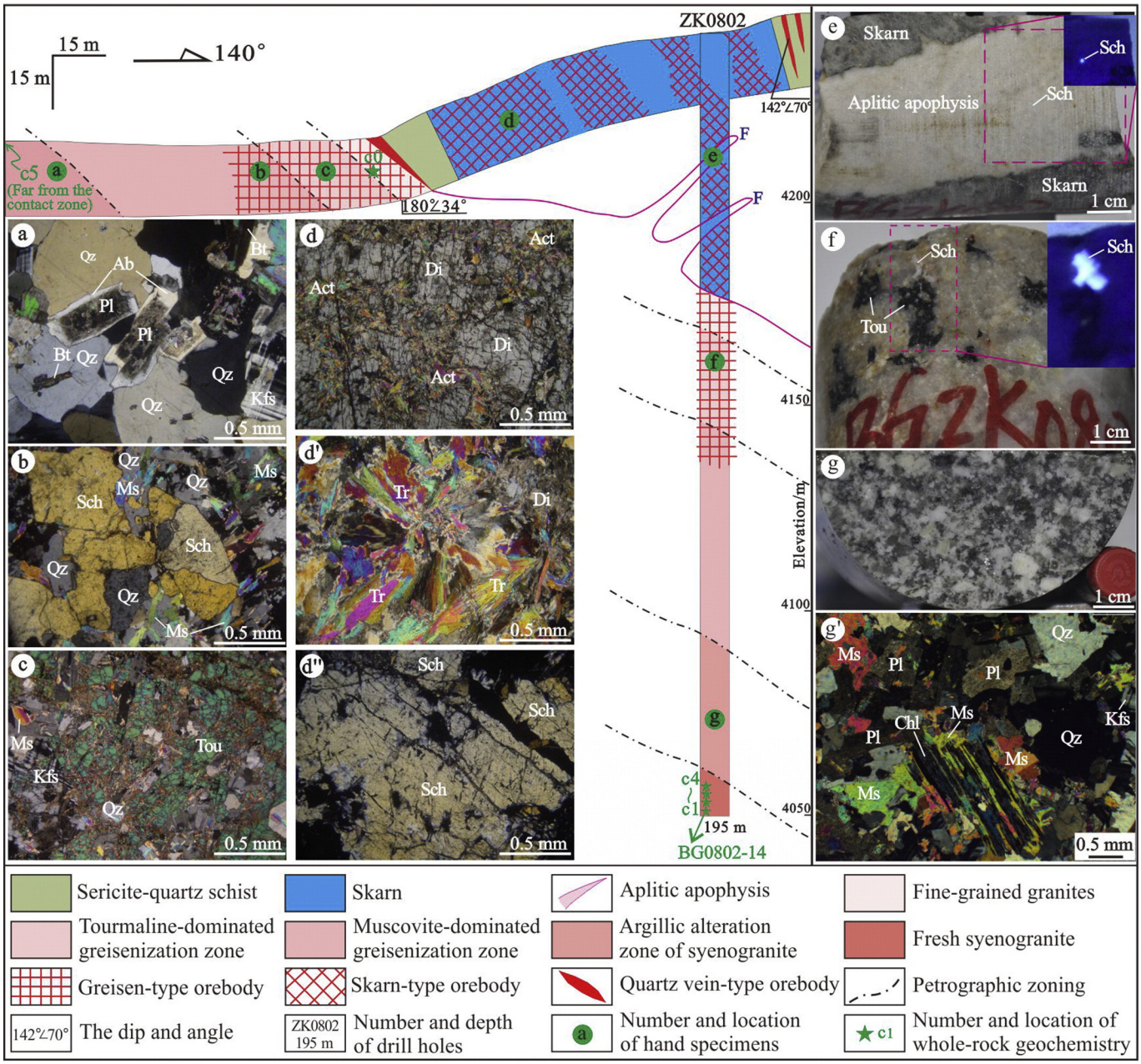

Fig. 7. Geological cross-section and photographs and photomicrographs (cross polarized light) from the Baiganhu W–Sn deposit (images at top right in (e) and (f) were taken under ultraviolet light). (a) Sericitization and argillization of feldspar. (b) Muscovite-dominated greisenization zone with scheelite. (c) Tourmaline-dominated greisenization zone. (d), (d′) and (d″) Main skarn minerals and associated scheelite (note the diopside replaced by actinolite and tremolite). (e) Aplitic apophysis with disseminated scheelite. (f) Tourmaline-dominated greisenization zone with scheelite. (g) and (g′) Argillic alteration zone with chloritization, sericitization, and argillization. Mineral abbreviations are as in Fig. 3.

The three types of W–Sn mineralization (skarn-, greisen-, and quartz-vein-type) constitute a W–Sn metallogenic series that is spatially associated with syenogranite in the Caledonian Bashierxi magmatic series and with metasediments of the Paleoproterozoic Xiaomiao Formation of the Jinshuikou Group.

3.2. Vertical zoning in alteration and mineralization

The nature of vertical zoning in petrography yields important insights into ore-forming processes, and is beneficial for assessing and exploring buried orebodies. We have identified seven petrographic zones (A–G, from roughly downward to upward) based on detailed observations of mineral assemblages and textures observed in samples from outcrops and core logging of numerous drill holes in the orefield (e.g., drill holes No. 14808, No. 14801, No. 14804, and No. 14805 in the Kekekaerde deposit, and No. 0802 in the Baiganhu deposit; Figs. 5, 7). The main features of the zones and related mineralization are presented briefly below, as exemplified by exploration line No. 148 in the Kekekaerde deposit and No. 08 in the Baiganhu deposit (Figs. 4–7).

(A) Fresh syenogranite zone.

In cross-section, fresh syenogranite is located mainly in the lowermost part of the Baiganhu deposit (drill hole No. 0802) (Fig. 7). The syenogranite is generally free of alteration and is marked by fresh magmatic biotite, muscovite, feldspar, quartz, apatite, and garnet. Rare W–Sn mineralization occurs in this zone.

(B) Argillic alteration zone.

The argillic alteration zone occurs at the bottom of the intrusion. As compared with the fresh syenogranite zone, the rocks in this zone are faded in color, and many of the biotite has disappeared. Some residual fragments of biotite occur as replacements of muscovite flakes or chlorite,

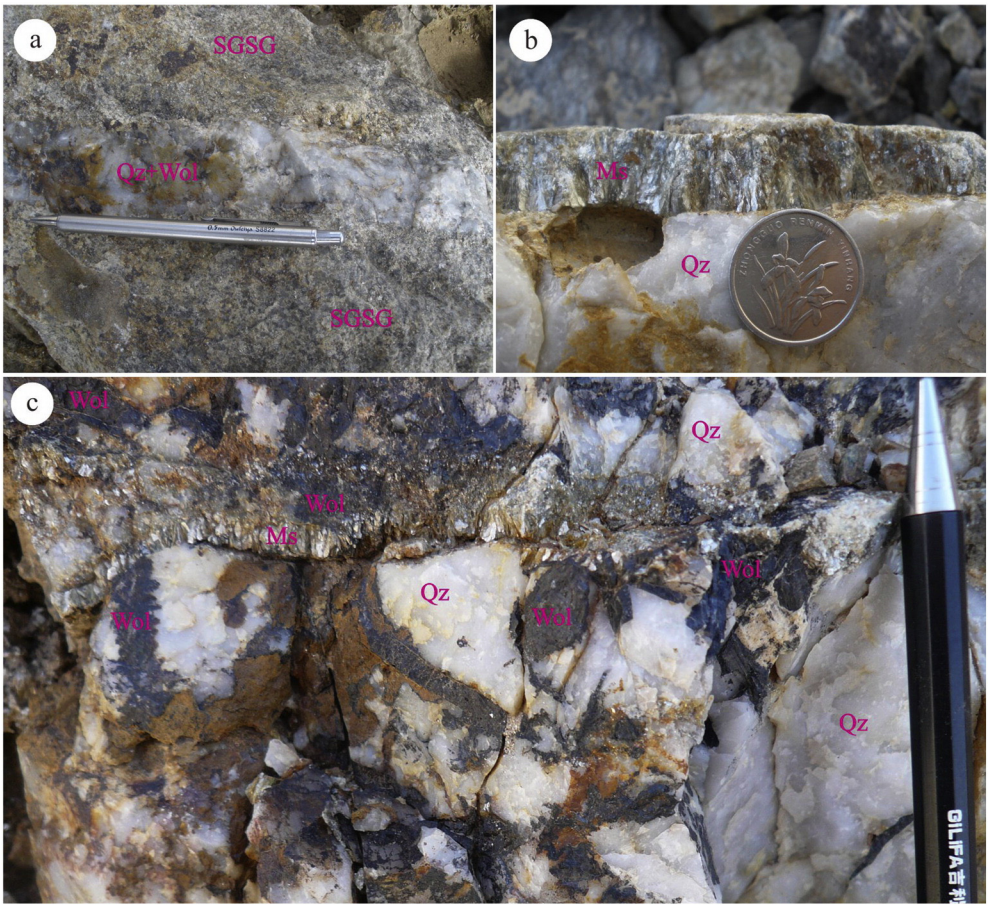

Fig. 8. Photographs showing hydrothermal muscovite associated with W–Sn mineralization in the Kekekaerde deposit. (a) Strongly greisenized syenogranite (SGSG) associated with W–Sn mineralization. (b) and (c) Wolframite-bearing quartz vein associated with hydrothermal muscovite. Mineral abbreviations are as in Fig. 3.

exhibiting the anomalous interference color Berlin Blue (Fig. 7g′). The cores of feldspar are commonly subject to argillation and sericitization. Locally, plagioclase is entirely replaced by pseudomorphs of sericite or clay minerals (Fig. 7a, g′). Carbonatization of plagioclase is also observed locally. The accessory minerals are basically the same as those in the fresh syenogranite zone. The mineralization in this zone consists mainly of disseminated pyrite and locally sphalerite and chalcopyrite; W–Sn-bearing ore minerals are rarely observed. A distinguishing mineralogical feature of this zone is the presence of residual biotite (dark in color), which is scarcely observed in the other zones described below.

(C) Muscovite-dominated greisenization zone.

The muscovite-dominated greisenization zone is developed mainly in the lower–middle portions of the intrusion. The rocks consist mainly of hydrothermal muscovite and quartz with rare occurrences of biotite or tourmaline (Figs. 6j,j′, 7b,g). Locally, the muscovite occurs as lepidoaggegrate, with individual crystal sizes of 3–5 mm. Accessory minerals in this zone are less abundant, but magmatic garnet inclusions in quartz are locally present (Fig. 6j′). In the upper part of the zone, fine-grained disseminated scheelite accompanied by muscovite + quartz ± feldspar assemblages is present, along with locally coarse-grained euhedral scheelite (Fig. 7b). The W–Sn mineralization gradually decreases and even vanishes in the lower parts of the zone, whereas mineralization in the form of quartz veins bearing pyrite ± chalcopyrite ± sphalerite ± pyrrhotite ± molybdenite and cross-cutting the greisen is common.

(D) Tourmaline-dominated greisenization zone.

The tourmaline-dominated greisenization zone is developed mainly in the middle–upper portions of the intrusion. The widespread presence of tourmaline as needle-like or columnar euhedral crystals disseminated in altered syenogranite or as nested aggregates accompanied by coarse-grained anhedral quartz is the main feature of this zone (Figs. 6i, 7c,f). The rocks consist mainly of the replacement minerals tourmaline, muscovite, quartz, and arsenopyrite, as well as residual K-feldspar, plagioclase, and quartz. Locally, needle-like or prismatic apatite is found associated with the residual feldspar. The apatite crystals are euhedral and 0.03–0.50 mm long. They are colorless under plane polarized light, and show mainly first-order gray but locally anomalous interference colors under cross-polarized light. A cathodoluminescence (CL) study by Breiter et al. (2002a) on the feldspar from four peraluminous granitic systems in Europe showed that the occurrence of small deuteric apatite grains within feldspar (strongly visible and often yellow in color under cathodoluminescence) is typical for altered peraluminous granites. In this zone of the present study, medium- to fine-grained anhedral scheelite is generally observed disseminated in the altered rock, and locally scheelite occurs as coarse euhedral crystals (Fig. 7f). Where the greisenized rock is cross-cut by wolframite ± cassiterite-bearing quartz veins, some wolframite grains are also distributed in the altered rock next to the quartz vein (Fig. 6h).

(E) Marginal facies zone.

The marginal facies zone occurs mainly along the margin or in the very upper parts of the intrusion. Two different petrographic facies have been recognized in this zone: (i) K-feldspar pegmatite, locally showing unidirectional solidification textures (USTs); and (ii) fine-grained granite, locally with miarolitic cavities.

The *marginal pegmatite* is characterized by light pink or white K-feldspar pegmatite, which occurs mainly along steep contacts between the intrusion and metasediments of the Xiaomiao Formation (Figs. 5, 6f,j). The K-feldspar megacrystals are generally 5–20 cm in size, and in places up to 25 cm; locally, they grow perpendicular to the contact zone, forming a specific type of UST. As mentioned above, the

pegmatites show several repetitions, with total thicknesses of 5–20 m and with individual layers 0.1–2.0 m thick. The pegmatites themselves are generally barren, but disseminated scheelite mineralization occurs in the later greisen phase of alteration. Although the occurrences of these pegmatites are similar to those in the Erzgebirge Mountains of Central Europe (Breiter et al., 2005), they differ in terms of their volatile components (Pollard et al., 1987), as the European varieties are B-poor granite–pegmatite systems (relatively rich in F and P but poor in B; Breiter et al., 2005), whereas the pegmatites in Baiganhu orefield are a B-rich granite–pegmatite system (with abundant tourmaline, and deficient in fluorite and topaz, as mentioned above).

The occurrence of "marginal pegmatite" as layers located immediately adjacent to the upper granite contact is one of the most typical features of Sn–W-bearing granites (Pollard et al., 1988; Breiter, 2002b; Breiter et al., 2005). Pegmatites are often the first products to form near contact planes from the crystallization of a parental granite melt during cooling, as described in the model of "undercooling of H_2O-rich melt" (Breiter et al., 2005 and references therein). According to Breiter et al. (2005), the repeated UST layers may have been produced by a periodic process involving a sudden adiabatic pressure drop during opening of the water-rich melt system, causing "undercooling" of the magma, followed by a pressure increase and restoration of the conditions of "standard" granitic crystallization.

Interestingly, a more recent study on the newly discovered world-class superlarge Dahutang W deposit in northwest Jiangxi Province, South China, also confirms the presence of a "pegmatoid shell" (Zhang et al., 2015), which is well developed above a mother rock of porphyritic biotite granite. A vertical section from the mother rock to the wall rock (granodiorite) shows the following sequence: porphyritic biotite granite, felsic aplite, quartz–feldspar pegmatoid, feldspar–quartz pegmatoid, and scheelite-bearing biotite granodiorite (Zhang et al., 2015).

The later *fine-grained granites* are preferentially distributed in the very upper part of the intrusion, and sometimes alternate with the aforementioned marginal K-feldspar pegmatites. Locally, these fine-grained granites possess irregularly shaped miarolitic cavities that are usually filled with crystals of euhedral feldspar and quartz (crystal size, 0.01–5.00 mm) (Fig. 6d). The miarolitic cavities, which are interpreted to form from vapor bubbles released from the granitic melt (Candela, 1997), are one of the typical features that characterize closed magmatic systems (Pirajno, 2009, page 218). These fine-grained granites locally show relatively high abundances of quartz resulting from quartz-dominated greisenization, and some disseminated scheelite mineralization occurs in the altered fine-grained granite.

(F) Aplitic apophysis zone.

The typical feature of the aplitic apophysis zone is the presence of aplitic apophyses (or dikes) that emanate from the pluton and intrude the metasediments above the cupola (Figs. 5, 7). The width of the apophyses is generally small (in the range of 0.02–2.00 m). Two types of apophyses have been recognized based on mineral assemblages: tourmaline-bearing apophyses and albite-bearing apophyses. The former characteristically consist of needle-like or columnar fine or medium- to fine-grained tourmaline (Fig. 6c,e), while the latter typically contain abundant fine-grained plagioclase with polysynthetic twins (mainly albite, as confirmed by electron microprobe analysis) (Fig. 7e). This zone, which is developed mainly in the wallrock (metasediments) above the cupola, provides a significant clue to the presence of the hidden intrusion and accompanying mineralization (Figs. 4, 5). Apart from the disseminated medium- to fine-grained scheelite mineralization, which commonly occurs in the apophyses (Fig. 7e), wolframite + muscovite ± cassiterite-bearing quartz veins are also usually developed in the contact zone between the apophyses and the metasediments of the Xiaomiao Formation (Fig. 5).

(G) Skarn zone (G1) and infilled silification zone (G2).

Rocks in the skarn zone are light green or gray-white in color (Fig. 6a), and generally show lepidoblastic textures with banded structures. This zone is characterized by skarn (Fig. 7d,d′), consisting of major diopside, tremolite, quartz, and actinolite, and minor garnet, idocrase, phlogopite, zoisite, clinozoisite, and calcite. The zone is interbedded with the major quartz–sericite schists adjacent to the intrusion (Figs. 5, 7). The skarn zone is rich in scheelite mineralization, which consists of medium to fine anhedral crystals disseminated in the skarn (Fig. 6a′), or occurs as coarse aggregates (Fig. 7d″) accompanied by diopside, tremolite, actinolite, quartz, and calcite.

Rocks in the infilled silification zone generally show vein or stockvein structures, and to a lesser extent massive structures. The infilled silification zone is developed mainly in the exocontact zone of sericite–quartz schist, and also in the endogreisen zone (Fig. 5). The ore-bearing quartz veins (described in the previous section) consist mainly of wolframite + muscovite ± cassiterite ± scheelite (Figs. 6b, 8). Barren quartz veins vary considerably in width, strike, and dip; the premineralization quartz veins seem to be generally more gently dipping than the ore-bearing quartz veins. The postmineralization quartz veins commonly contain fluorite and calcite.

3.3. Paragenetic relationships

Paragenetic studies based on mineral assemblages and cross-cutting relationships indicate five main alteration–mineralization stages in the orefield: (I) skarn stage, (II) greisen stage, (III) quartz vein stage, (IV) argillitic alteration stage, and (V) supergene stage. The paragenesis of the alteration and mineralization is presented in Fig. 9, and the main mineral assemblages and features are described briefly below.

(I) Skarn stage.

The skarn stage is represented mainly by calc-magnesian skarn and three different mineral assemblages. From early to late, the three mineral assemblages represent the early substage (II_1), characterized by large amounts of diopside and minor garnet; the middle substage (II_2), which overprints the early substage (II_1) (Fig. 7d,d′) and consists of tremolite, actinolite, scheelite, quartz, and phlogopite; and the late substage (II_3), which is characterized by zoisite, clinozoisite, and quartz as the major minerals. Among the three substages, the middle substage (II_2) is the predominant period of scheelite mineralization.

(II) Greisen stage.

Locally, some greisen stringers (0.1–0.5 mm in width and consisting mainly of quartz and muscovite) cross-cut the skarn mineral assemblages (e.g., diopside and tremolite), which indicates that the greisenization and related mineralization occurred later than in the skarn stage. Three different mineral assemblages (from early to late) are associated with the W–Sn mineralization of this stage, as follows:

(II_1) quartz (dominant) + muscovite ± albite ± tourmaline ± scheelite ± wolframite,

(II_2) tourmaline (dominant) + quartz + muscovite ± scheelite ± wolframite ± apatite ± arsenopyrite,

(II_3) muscovite (dominant) + quartz ± scheelite ± pyrite ± pyrrhotite ± molybdenite ± fluorite.

(III) Quartz vein stage.

In the orefield, three types of quartz veins (from early to late) have been recognized. The Type 1 veins (III_1), as mentioned previously, occur mainly in the exocontact zone in metasediments or in the upper portions of the cupola; the veins contain large amounts of W–Sn-bearing ore minerals. The Type 2 veins (III_2) locally cut the Type 1 veins (III_1), and mainly contain minor Cu/Zn/Mo mineralization. The Type 3 veins (III_3) contain fluorite and calcite, and occur mainly in the lower part of the intrusion. The vein mineral assemblages are as follows:

(III_1) quartz + wolframite + muscovite ± cassiterite ± scheelite ± K-feldspar (Figs. 6b, 8b,c),

(III_2) quartz + pyrite ± chalcopyrite ± molybdenite ± sphalerite,

(III_3) quartz + fluorite + calcite.

The strongly greisenized syenogranites are commonly cut by the quartz veins, especially the Type 1 veins (III_1, Fig. 8a), which locally also extend into the surrounding metasediments (Fig. 5).

(IV) Argillic alteration stage.

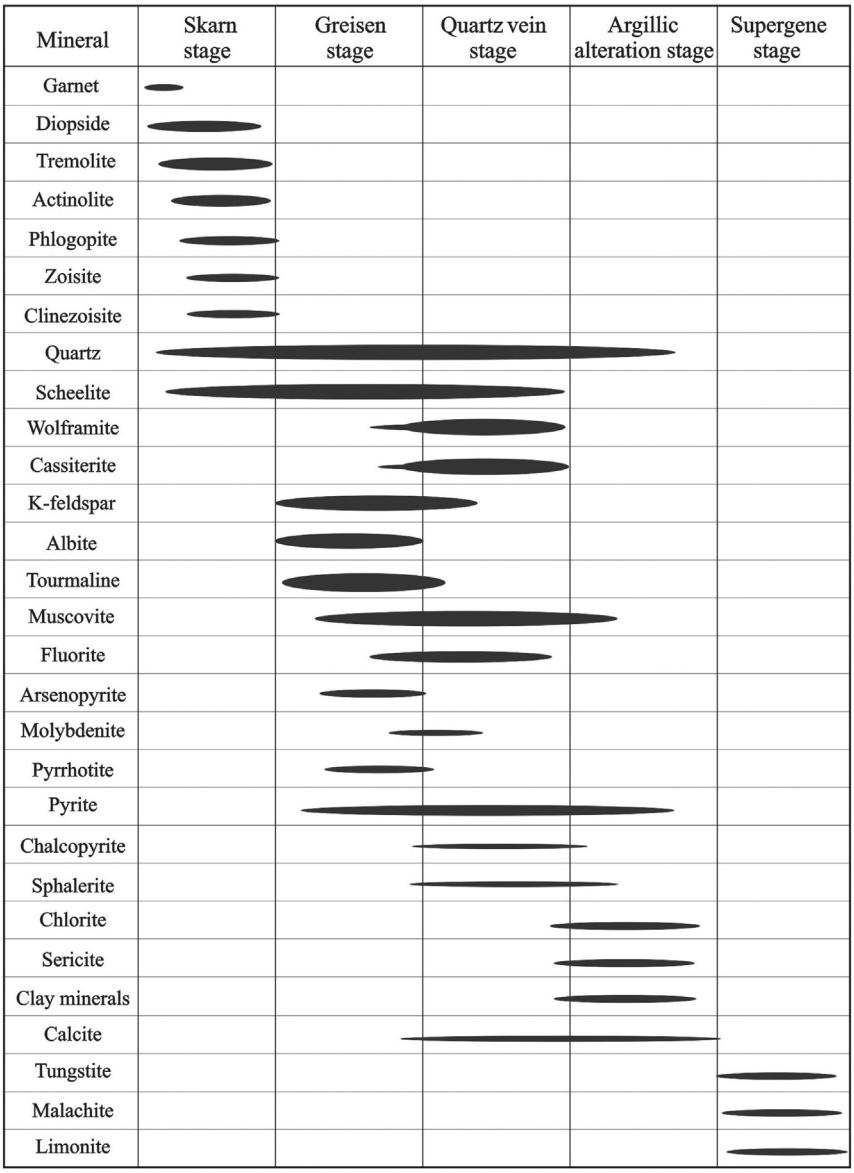

Fig. 9. Paragenesis of the main alteration and mineralization phases in the Baiganhu W–Sn orefield.

The argillic alteration stage is characterized by alteration phases such as chlorite, sericite (locally muscovite), calcite, and clay minerals, together with residual biotite and feldspar. The W–Sn-bearing ore minerals of this stage are rarely observed, but disseminated or veinlet-type pyrite, sphalerite, and chalcopyrite are common.

(V) Supergene stage.

The supergene stage is typified by the oxidization of pre-existing minerals, such as wolframite, chalcopyrite, and pyrite, which have been oxidized to tungstite (yellow–green in color), malachite, and limonite, respectively, on the surface or in fractures. These oxidized minerals are signatures of the hidden primary orebody.

The above five stages generally represent the evolution of alteration–mineralization processes in the orefield. Due to the complexity of the hydrothermal fluids, the stages, especially the substages, are not completely isolated from one another, and likely overlapped with one another temporally. Based on zoning and paragenetic relationships of the alteration–mineralization assemblages, reversal alteration zoning is thought to exist in the deposits. That is, the relatively high-temperature oxide minerals, such as wolframite, cassiterite, and scheelite, as well as accompanying alteration phases, occur mainly in shallow environments, while the relatively low-temperature sulfide minerals, such as pyrite, chalcopyrite, pyrrhotite, and sphalerite, together with related alteration phases, typically occur at depth.

4. Analytical results

We present mineral chemical, whole-rock geochemical, and zircon U–Pb–Hf data, together with hydrothermal muscovite ^{40}Ar–^{39}Ar ages for rocks and minerals in the orefield. The pertinent analytical methods and data processing procedures are described in the Supplementary Materials.

4.1. Mineral compositions

Representative electron microprobe analyses and calculated parameters for the magmatic minerals are listed in Table S1 in the Supplementary Materials.

Hornblende (H1–H3) in the fresh monzogranite in the northeast part of the orefield (Fig. 3b) consists mainly of SiO_2 (~41%), FeO (~28%), CaO (~10%), Al_2O_3 (~9%), and minor amounts of MgO (2%–3%), Na_2O (1%–2%), and K_2O (1%–2%). Based on International Mineralogical Association recommendations for amphibole nomenclature

Table 1
Geochemical compositions and parameters of the parental syenogranite (major elements are presented in wt.%; trace elements are presented in ppm).

Lithology	Fresh syenogranite from the bottom of drill hole No. 0802				Fresh syenogranite from the outcrop	Strongly greisenized syenogranite from the outcrop
Sample number	c1	c2	c3	c4	c5	c0
SiO_2	72.27	71.31	71.57	71.10	71.88	85.24
TiO_2	0.25	0.26	0.29	0.26	0.30	0.14
Al_2O_3	14.35	14.57	14.80	14.55	13.84	8.54
Fe_2O_3	0.46	0.42	0.46	0.39	0.87	0.39
FeO	1.42	1.38	1.56	1.85	1.70	0.65
MnO	0.07	0.07	0.08	0.1	0.12	0.07
MgO	0.63	0.64	0.71	0.64	0.71	0.32
CaO	1.87	1.83	2.06	1.97	1.79	0.28
Na_2O	3.29	3.32	3.62	3.33	3.32	0.27
K_2O	4.03	4.03	3.71	4.23	3.54	2.66
P_2O_5	0.10	0.12	0.11	0.11	0.13	0.09
LOI	1.65	1.70	1.47	1.44	1.77	1.34
Total	100.39	99.65	100.44	99.97	99.97	99.99
$K_2O + Na_2O$	7.32	7.35	7.33	7.56	6.86	2.93
K_2O/Na_2O	1.22	1.21	1.02	1.27	1.07	9.85
σ	1.83	1.91	1.88	2.03	1.63	0.20
A/CNK	1.09	1.11	1.08	1.07	1.10	2.23
A/NK	1.47	1.48	1.48	1.45	1.49	2.57
W	113.0	51.8	39.1	69.5	55.6	301.0
Sn	23.0	24.9	23.1	26.0	34.0	0.6
La	19.5	20.1	22.2	21.7	26.2	11.6
Ce	41.6	40.9	46.6	43.5	51.4	23.1
Pr	4.77	4.97	5.55	5.32	5.97	2.53
Nd	18.10	19.30	21.20	19.80	21.00	9.84
Sm	4.03	4.28	4.75	4.35	4.70	2.09
Eu	0.60	0.58	0.68	0.71	0.85	0.20
Gd	4.04	4.19	4.75	3.90	4.43	1.93
Tb	0.68	0.73	0.80	0.83	0.85	0.34
Dy	3.63	4.11	4.28	4.42	4.70	1.79
Ho	0.72	0.81	0.79	0.76	1.02	0.35
Er	2.08	2.33	2.29	2.41	2.86	0.93
Tm	0.33	0.35	0.36	0.47	0.50	0.18
Yb	2.12	2.50	2.45	2.89	3.02	1.14
Lu	0.31	0.37	0.36	0.40	0.43	0.15
TREE	102.51	105.52	117.06	111.45	127.92	56.17
LREE	88.6	90.13	100.98	95.38	110.12	49.36
HREE	13.91	15.39	16.08	16.08	17.81	6.81
LREE/HREE	6.37	5.86	6.28	5.93	6.18	7.24
$(La/Yb)_N$	6.37	5.86	6.28	5.93	6.18	7.30
$(La/Sm)_N$	3.13	3.04	3.02	3.22	3.60	3.58
$(Gd/Yb)_N$	1.58	1.39	1.60	1.12	1.21	1.40
δEu	0.45	0.41	0.43	0.51	0.56	0.29
δCe	0.45	0.41	0.43	0.51	0.56	1.00
Rb	257	267	250	305	257	272
Ba	283	308	300	376	292	177
Y	19.70	21.60	21.60	23.40	26.60	9.47
Th	9.61	10.10	11.90	12.00	13.00	8.93
U	7.84	8.93	6.93	7.26	5.34	2.30
Ta	4.32	4.44	3.75	3.61	2.72	1.50
Nb	14.20	13.80	17.20	16.50	17.50	8.26
Sr	173	182	159	244	208	23
Zr	100	119	116	152	168	141
Hf	3.61	4.10	4.08	5.24	5.59	4.57
Pb	22.7	24.5	24.2	28.2	21.7	295.0
Ga	17.25	18.38	19.06	16.00	15.80	14.50
Zn	60.4	63.7	62.8	61.4	74.1	21.4
10,000*Ga/Al	2.27	2.38	2.43	2.08	2.16	3.21
Ce + Zr + Y + Nb	175.50	195.30	201.40	235.40	263.50	181.83
T_{Zr} (°C)	751	765	764	784	791	–

Notes:
LOI is loss of ignition; K_2O/Na_2O (mass ratio); σ (The Rittmann Index) = $(Na_2O + K_2O)^2/(SiO_2 - 43)$ (the oxide in wt.%); A/CNK = $Al_2O_3/(CaO + Na_2O + K_2O)$ (molar ratio); A/NK = $Al_2O_3/(Na_2O + K_2O)$ (molar ratio).
TREE, total rare earth elements; LREE, light rare earth elements; HREE, heavy rare earth elements.
$(La/Yb)_N = (La/La^*)/(Yb/Yb^*)$; $(La/Sm)_N = (La/La^*)/(Sm/Sm^*)$; $(Gd/Yb)_N = (Gd/Gd^*)/(Yb/Yb^*)$.
$\delta Eu = (Eu/Eu^*)/\{0.5 \times [(Sm/Sm^*) + (Gd/Gd^*)]\}$; $\delta Ce = (Ce/Ce^*)/\{0.5 \times [(La/La^*) + (Pr/Pr^*)]\}$.
The normalized values of La*, Ce*, Pr*, Sm*,Eu*, Gd*, Yb* according to Sun and McDonough, 1989.
T_{Zr} (°C) = 12,900/(2.95 + 0.85 × M + $\ln D^{Zr,\ zircon/melt}$) (Watson and Harrison, 1983), where $D^{Zr,\ zircon/melt}$ is the ratio of Zr concentrations (ppm) in zircon to that in the saturated melt, M = cation ratio (Na + K + 2 × Ca)/(Al × Si). The geothermometer is calibrated for M = 1.32 to 1.39.

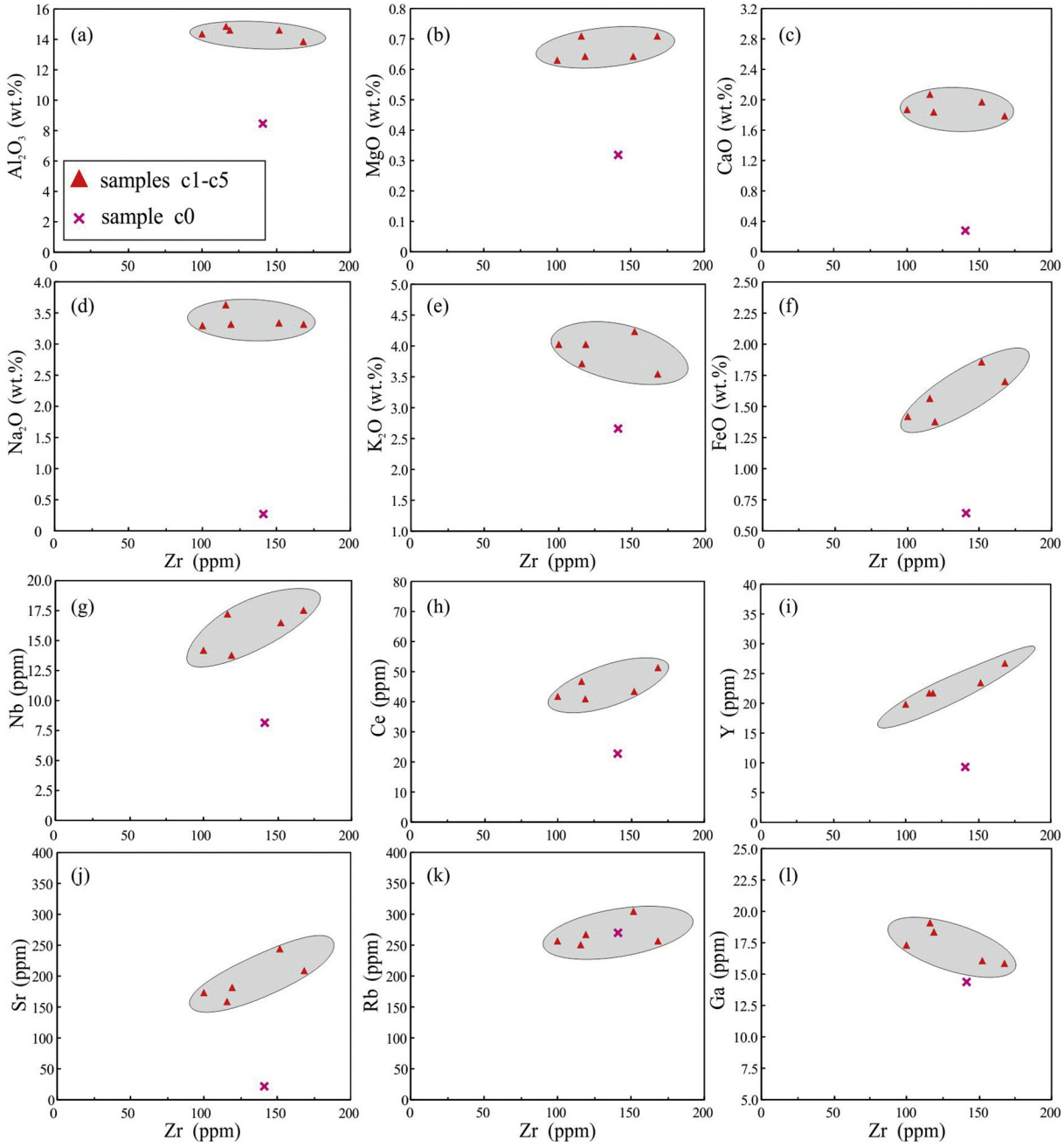

Fig. 10. Covariation diagrams of Zr versus selected major oxides (a–f) and trace elements (g–l) for the syenogranite samples from Baiganhu W–Sn deposit; samples c1–c5 are least altered (i.e., fresh) syenogranite; sample c0 is strongly greisenized.

(Hawthorne et al., 2012), all three samples constitute ferro-pargasite (calcium amphiboles).

Garnet (G1–G3) in the fresh syenogranite in the Baiganhu deposit (Fig. 3f) exhibits high contents of MnO_2 (24%–26%) and FeO (~15%), and low contents of CaO and MgO (both <1%). The abundances of SiO_2 and Al_2O_3 in the garnet are relatively constant (36%–37% and 20%–22%, respectively). The garnet is composed mainly of a solid solution of almandine–spessartine (36%–38 mol% and 61%–63 mol%, respectively).

Garnet (G4–G6) in the altered syenogranite (Fig. 6j′) in the Kekekaerde deposit has nearly the same chemical composition as the garnet in the fresh syenogranite in the Baiganhu deposit, except that the FeO contents of the Kekekaerde deposit garnet are slightly higher. The chemical features of the garnets in both deposits are consistent with those of magmatic garnet in the Xihuashan granites (Yang et al., 2013). The magmatic garnets in both deposits also indicate that the parental granites are peraluminous.

Biotite (B1–B3) in the fresh syenogranite (Fig. 3e) is relatively rich in Fe, with Fe/(Fe + Mg) ratios of 0.606–0.620; the composition is analogous to that of biotite in the Dahutang granites, which host the newly discovered Dahutang W deposit (Huang and Jiang, 2014).

Plagioclase (P1–P3) in the fresh syenogranite varies from An_{15} to An_{19}, and K-feldspar (K1–K3) in the fresh syenogranite has orthoclase contents of 93–98 mol%, with minor albite contents (2–7 mol%) and rare anorthite.

4.2. Whole-rock geochemistry

4.2.1. Alteration effects

The whole-rock major and trace element compositions of the fresh syenogranite samples (c1–c5) and the one strongly greisenized syenogranite sample (c0) from the Baiganhu deposit are listed in Table 1. To consider the possible influence of alteration on the parental

syenogranite, it is necessary to assess the mobility of major and trace elements prior to interpretation of the geochemical data. Zirconium is considered to be one of the least mobile elements, and is commonly used as an alteration-independent index of geochemical variations (Pearce et al., 1992). On binary diagrams of major oxides (Al_2O_3, MgO, CaO, Na_2O, K_2O, and FeO) and trace elements (Nb, Ce, Y, Rb, Sr, and Nb) versus Zr, all five fresh syenogranite samples show co-linear trends (Fig. 10), indicating the immobility of chemical elements after magma emplacement (Wang et al., 2012); this immobility is confirmed by microscope observations of only rare replacement of rock-forming minerals. The conclusion that elements were relatively immobile after magma emplacement is also supported by the generally low loss on ignition (LOI) values (1.44%–1.77%), and is consistent with trace element patterns (Fig. 11c) (Polat et al., 2002). Consequently, the five fresh syenogranite samples are considered to preserve their original concentrations of almost all major oxides and trace elements, which are hence used in the ensuing discussion.

The strongly greisenized syenogranite sample (c0), on the other hand, shows departures from the co-linear trends observed for the fresh syenogranites on the binary diagrams (with the exception of Rb vs. Zr and Ga vs. Zr; Fig. 10). In addition, the replacement of rock-forming minerals such as K-feldspar and plagioclase by large amounts of quartz and muscovite, as observed under the microscope, is quite common. Consequently, the characteristics of the strongly greisenized syenogranite sample cannot be used to discuss the genetic type, petrogenesis, or related tectonic setting of the parental syenogranite.

4.2.2. Major element geochemistry

The major element contents of the syenogranite samples from the Baiganhu deposit are listed in Table 1. The fresh samples (c1–c5) show relatively high SiO_2 contents (71.10%–72.27%), ($K_2O + Na_2O$) values of 6.86%–7.56% (average, 7.28%), and Rittmann index ($\sigma = (Na_2O + K_2O)^2 / (SiO_2 - 43)$ (oxides in wt.%)) values of 1.63–2.03. On a K_2O–SiO_2 diagram, the samples plot in the high-K calc-alkaline field (Fig. 11a). The (K_2O)/(Na_2O) ratios (oxides in wt.%) of the syenogranites are 1.07–1.27 (average, 1.16), and the contents of CaO, MgO, and Al_2O_3 are 1.79%–2.06%, 0.63%–0.71%, and 13.84%–14.80%, respectively. The Shands index (A/CNK) values are 1.07–1.11, indicating that the syenogranites are peraluminous (Fig. 11b), which is consistent with the presence of magmatic garnet and muscovite.

For comparison, five samples of fresh monzogranite (a1–a5; Li et al., 2012a) and eight samples of fresh alkali feldspar granite (b1–b3, Gao and Li, 2011; b4–b8, Li et al., 2012a) from outcrops in the northeast of the Kekekaerde deposit, together with five samples of fresh syenogranite (c6–c10, Wang et al., 2014b) from outcrops in the Bashierxi deposit are also plotted in Fig. 11; their major and trace element geochemical features (summarized in Table 3) are briefly described in this and a later section. The fresh syenogranites (c6–c10) cropping out in the Bashierxi deposit also contain garnet and muscovite of magmatic origin (Wang et al., 2014b), and show major element features that are generally shared with the fresh syenogranites of the Baiganhu deposit (this study) (Fig. 11a,b). However, the fresh monzogranites (a1–a5) and the alkali feldspar granites (b1–b8) show much higher alkali contents (9.54%–9.69% and 8.30%–9.38%, respectively) and lower A/CNK values (0.92–0.94 and 0.95–1.02, respectively); thus, they belong to the metaluminous or slightly peraluminous shoshonite series (Fig. 11a,b).

4.2.3. Trace element geochemistry

Trace element data of the syenogranites from the Baiganhu deposit are also listed in Table 1. The fresh syenogranites (c1–c5) show moderate contents of total rare earth elements (TREEs = 103–128 ppm) and

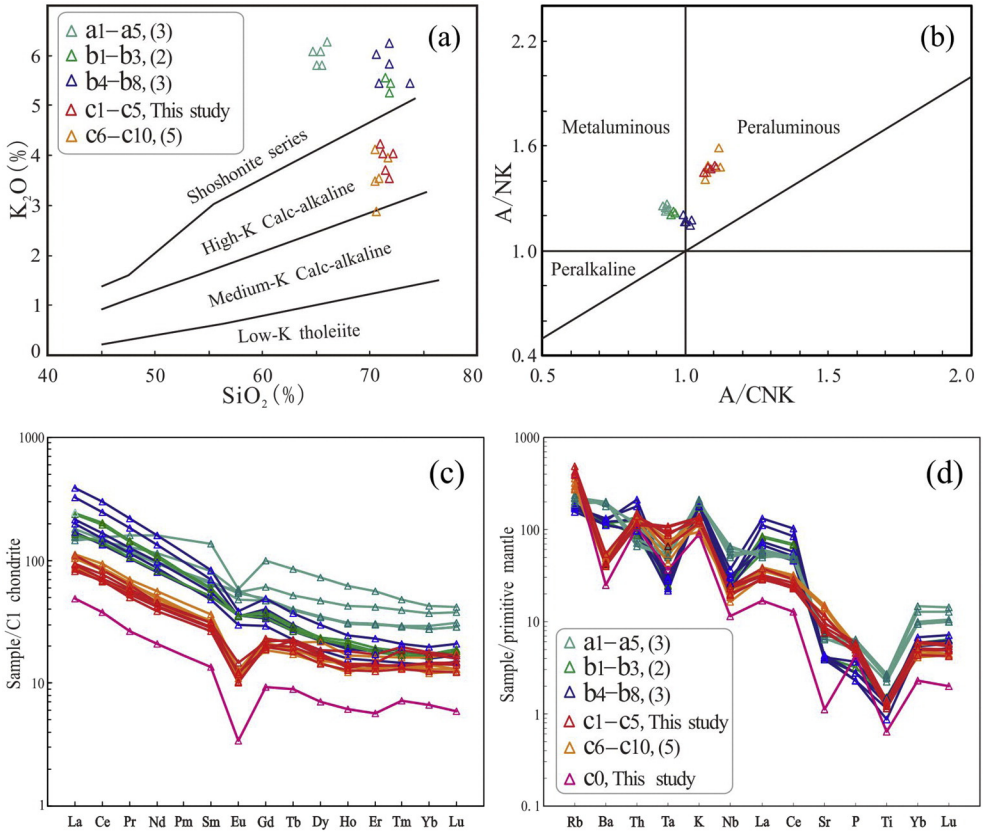

Fig. 11. Major and trace element features of the granitoids of the Bashierxi magmatic series. (a) SiO_2 vs. K_2O (Rollinson, 1993). (b) A/CNK vs. A/NK (Maniar and Piccoli, 1989). (c) Chondrite-normalized rare earth element (REE) patterns. (d) Primitive-mantle-normalized spider diagram (chondrite and primitive mantle values are from Sun and McDonough, 1989). Symbols and references are the same as in Fig. 2; see text for details.

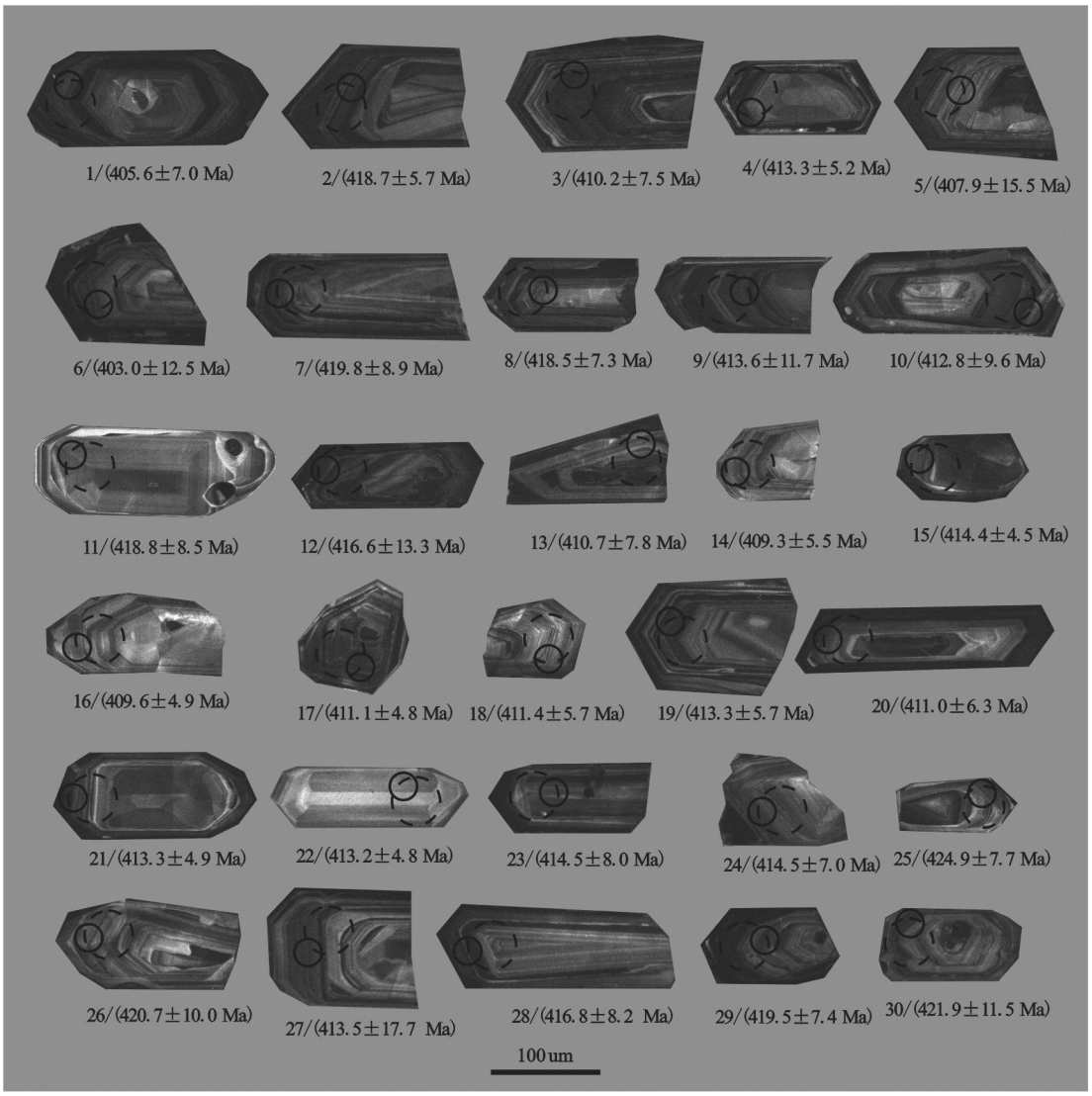

Fig. 12. Cathodoluminescence (CL) images of zircons from the parental syenogranite (BG0802-14) in the Baiganhu W–Sn deposit. Smaller circles denote the locations of U–Pb dating, whereas larger dotted circles show the positions of Lu–Hf analyses.

are enriched in light rare earth elements (LREEs) and depleted in heavy rare earth elements (HREEs), with LREE/HREE ratios of 5.86–6.37, $(La/Yb)_N$ ratios of 5.39–6.60, and $(Gd/Yb)_N$ ratios of 1.12–1.60 (average, 1.38). In addition, chondrite-normalized REE patterns (Fig. 11c) display LREE enrichment and moderately negative Eu anomalies (δEu = 0.41–0.56; average, 0.47). On a primitive-mantle-normalized spider diagram, all five samples (c1–c5) show spikes in Rb, Th, U, and K, and troughs in Ba, Ta, Nb, and Ti (Fig. 11d). All trace element features of the five samples (c1–c5) in the Baiganhu deposit are consistent with those of the fresh syenogranites (c6–c10) exposed in the Bashierxi deposit (Fig. 11c,d).

The strongly greisenized syenogranite from the Baiganhu deposit (sample c0) (Fig. 7) shows a REE pattern and spider diagram (Fig. 11c,d) that are nearly the same as those of the fresh syenogranites (c1–c10), in spite of its lower LREE and HREE contents (49.36 ppm and 6.81 ppm, respectively) and stronger negative Eu (δEu = 0.29) and Sr anomalies.

The fresh monzogranites (a1–a5) and alkali feldspar granites (b1–b8) also show REE patterns (Fig. 11c) that are generally parallel to those of the fresh syenogranites (c1–c10). However, both the monzogranites and the alkali feldspar granites have higher TREE contents (247 ppm and 271 ppm, respectively), especially higher LREE contents, weaker negative Eu anomalies (δEu = 0.81 and 0.74, respectively), and generally steeper slopes in REE patterns (Fig. 11c). On a spider diagram (Fig. 11d), the monzogranites and alkali feldspar granites show, to some extent, patterns that are different than those of the fresh syenogranites (c1–c10), with weaker negative (or slightly positive) Ba anomalies and much stronger positive K, La, Ce, Yb, and Lu anomalies (Fig. 11d).

The contents of W and Sn in the fresh syenogranites (c1–c5) are unusually high (typically several tens of ppm) (Table 1), and are much higher than average upper crustal and lower crustal values (1.9 ppm and 0.6 ppm for W, and 2.1 ppm and 1.7 ppm for Sn, respectively; Rudnick and Gao, 2014). These values are also much higher than the available Sn contents in the fresh alkali feldspar granites and monzogranites (3.90–4.14 ppm, Gao and Li, 2011). The strongly greisenized syenogranite (c0) shows relatively high W contents but low Sn contents (Table 1), which were probably the result of the occurrence of greisen-type scheelite mineralization but not Sn mineralization in this altered rock.

4.3. Zircon U–Pb–Hf system

4.3.1. Zircon U–Pb geochronology

The majority of zircons extracted from the fresh syenogranite (BG0802-14; 37°56′13″N, 88°54′44″E) in the Baiganhu deposit are euhedral, 100–250 μm in length, and have length-to-width ratios of

2:1 to 3:1. Most of the zircons are transparent, colorless to slightly brown, and commonly show euhedral concentric zoning (Fig. 12), although some inherited zircons are also present.

We analyzed 30 magmatic zircons from the syenogranite (Table S2). Concentrations of U vary widely (391–4388 ppm), concentrations of Th are 158–1792 ppm, and Th/U ratios are 0.17–0.71. Age determinations based on U–Pb isotopic results show a single concordant group with a weighted mean ^{206}Pb–^{238} U age of 413.6 ± 2.4 Ma (MSWD = 0.36) (Fig. 13a), which is interpreted as the crystallization age of the syenogranite.

4.3.2. Zircon Hf isotope compositions

The in situ zircon Hf isotopic data for sample BG0802-14 are listed in Table S3 and shown in Fig. 13. The $^{176}Lu/^{177}Hf$ ratio (based on 30 analyses) is 0.000387–0.001740, and the $^{176}Hf/^{177}Hf$ ratio is 0.282285–0.282489 (average, 0.0282420). The calculated $\varepsilon_{Hf}(t)$ is between −8.5 and −1.1 (weighted mean, −3.8 ± 1.7) (Fig. 13c). The two-stage Hf model age (T^C_{DM}) is 1467–1931 Ma; an age peak occurs at 1550–1700 Ma (Fig. 13d).

For comparison, in situ zircon Hf isotopic data from the ca. 430.5 Ma fresh alkali feldspar granite (Gao and Li, 2011), obtained by the same analytical procedure, is also shown in Fig. 13. The calculated $\varepsilon_{Hf}(t)$ is between −2.3 and +5.6 (average, +1.5, Fig. 13c), and the two-stage Hf model age (T^C_{DM}) is 1059–1556 Ma, with an age peak at 1250–1400 Ma (Fig. 13d).

These data show that the parental magma of both the syenogranite and the alkali feldspar granite probably originated from partial melting of an old crustal component, although the source of the alkali feldspar granite is likely to have involved certain contributions of new crustal material.

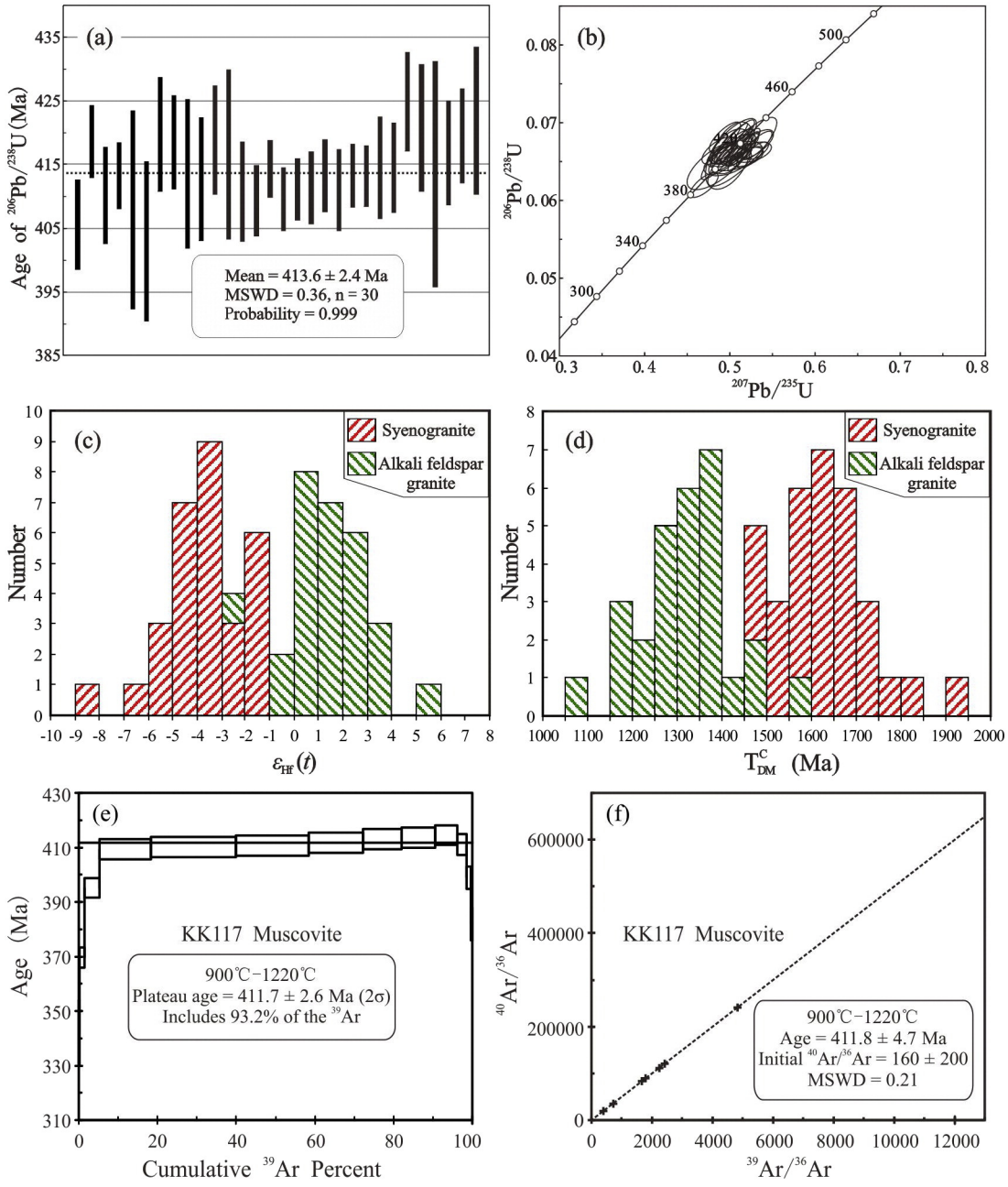

Fig. 13. Zircon U–Pb weighted average ages (a) and concordia ages (b) for the parental syenogranite (BG0802-14). (c) Histograms of $\varepsilon_{Hf}(t)$ values and (d) two-stage model ages (T^C_{DM}) for the ca. 413.6 Ma parental syenogranite (BG0802-14) and the ca. 430.5 Ma alkali feldspar granite (Gao and Li, 2011). (e) Incremental heating $^{40}Ar/^{39}Ar$ age spectra and (f) $^{40}Ar/^{36}Ar$–$^{39}Ar/^{36}Ar$ isochrons for hydrothermal muscovite (KK117).

4.4. Muscovite ^{40}Ar–^{39}Ar dating

The results ^{40}Ar–^{39}Ar analyses of hydrothermal muscovite from the Kekekaerde deposit are presented in Table S4. The analyzed samples were obtained from a strongly greisenized W–Sn mineralized syenogranite (KK117; 37°57′30″N, 88°56′23″E), a wolframite-bearing quartz vein with muscovite growing vertically along the walls of the vein (KK122; 37°57′36″N, 88°56′24″E), and a wolframite-bearing quartz vein with muscovite intergrowing with wolframite and quartz (KK140; 37°57′28″N, 88°56′26″E). The step-heating age spectrum and isochron for sample KK117 are shown in Fig. 13. The age spectrum shows a flat plateau representing more than 93.2% of the $^{39}Ar_K$ released during the sequence of eight successive heating steps (900 °C–1220 °C), indicating that K and radiogenic $^{40}Ar^*$ in the sample are distributed relatively homogeneously, and that K–Ar isotopic systematics were not affected by heating disturbances over the geological history of the sample. The eight successive steps (900 °C–1220 °C) yielded a well-defined weighted plateau age of 411.7 ± 2.6 Ma, an $^{39}Ar/^{36}Ar$–$^{40}Ar/^{36}Ar$ isochron age of 411.8 ± 4.7 Ma, and an initial $^{40}Ar/^{36}Ar$ ratio of 160 ± 20 (MSWD = 0.21; Fig. 13e,f).

The age spectra for samples KK122 and KK140 also yield well-defined weighted plateau ages of 412.8 ± 2.4 Ma and 413.8 ± 2.6 Ma, respectively, and $^{39}Ar/^{36}Ar$–$^{40}Ar/^{36}Ar$ isochron ages of 414.6 ± 3.9 Ma and 414.0 ± 4.0 Ma, respectively, with initial $^{40}Ar/^{36}Ar$ ratios of 209 ± 30 (MSWD = 0.22) and 247 ± 55 (MSWD = 0.46), respectively.

The initial $^{40}Ar/^{36}Ar$ ratio for each sample is close to the atmospheric value of 295.5 ± 0.5 (given by Steiger and Jager, 1977), indicating no excess argon in the samples. The weighted plateau ages are within error of the $^{39}Ar/^{36}Ar$–$^{40}Ar/^{36}Ar$ isochron ages, indicating that the ^{40}Ar–^{39}Ar dating results are reliable and are a good representation of the W–Sn mineralization ages of the Kekekaerde deposit.

5. Discussion

5.1. Age of the Bashierxi magmatic series

Zircon U–Pb dating by LA-ICP-MS gives a crystallization age of the syenogranite (BG0802-14) in the Baiganhu deposit of 413.6 ± 2.4 Ma (MSWD = 0.36, n = 30), which suggests that the magma was emplaced during the late Silurian and Early Devonian. The ages of other intrusions in the Bashierxi magmatic series obtained in recent studies are listed in Table 2 and shown in Fig. 2. Crystallization ages of a monzogranite cropping out in the northeast part of the orefield have been reported as 458.0 ± 9.0 Ma (Gao et al., 2010) and 421 ± 3.7 Ma (Li et al., 2012a), and ages for an alkali feldspar granite in the same area have been reported as 432.3 ± 0.8 Ma (Bao et al., 2008), 430.5 ± 1.2 Ma (Gao and Li, 2011), and 422 ± 3 Ma (Li et al., 2012a). Emplacement ages of the syenogranite cropping out in the Baiganhu and Bashierxi deposits have been reported as 428.2 ± 4.2 Ma and 422.5 ± 2.3 Ma, respectively (Wang et al., 2014b). An age of 416.9 ± 2.9 Ma for a granite (syenogranite?) associated with W–Sn mineralization in the Kekekaerde deposit has also been obtained (Sun et al., 2009). Our age data, in combination with the previously published data, indicate that the magmatism responsible for the Bashierxi magmatic series occurred mainly at ca. 432–413 Ma, and showed a near-contemporaneous evolutionary trend from the monzogranites and alkali feldspar granites (ca. 432–421 Ma) to the syenogranites (ca. 428–413 Ma). The age of 413.6 ± 2.4 Ma obtained in this study for the parental syenogranite is also within error of the age of 416.9 ± 2.9 Ma obtained for a parental granite by SHRIMP zircon U–Pb dating (Sun et al., 2009); both of these ages are the youngest ages obtained for the Bashierxi magmatic series, and thus indicate that the parental syenogranite magmatic event and related W–Sn mineralization probably took place during a relatively late stage of activity of the Bashierxi magmatic series.

5.2. Genetic type of the granitoids in the Bashierxi magmatic series

The fresh syenogranite (samples c1–c5 and c6–c10 collected from outcrops of the Baiganhu and Bashierxi deposits, respectively) contain magmatic garnet (almandine–spessartine) and geochemically are peraluminous and show elevated amounts of Al, K, and Rb, but are relatively depleted in Ca, Sr, and HREEs (Fig. 11; Table 1); these features are typical of S-type granites (Chappell and White, 1992, 2001; Collins and Richards, 2008; Champion and Bultitude, 2013). Also, the syenogranites exhibit low 10,000 × Ga/Al ratios (2.08–2.44) and low total Ce + Zr + Y + Nb contents (176–263 ppm) (Fig. 14a,b). On S- and I-type granite discrimination diagrams (White and Chappell, 1977), all of the syenogranites (c1–c10) plot in the S-type granite

Table 2
Isotopic ages and genetic types of the granitoids in the Bashierxi magmatic series, together with hydrothermal muscovite ^{40}Ar–^{39}Ar ages.

Sample	Age (Ma)	Genetic type	Analytical method	Sample location	Data source
Monzogranite (MG)	458.0 ± 9.0 (MSWD = 4.6, n = 15)	A	Zircon U–Pb LA-ICP-MS	N38°00′0.5″ E89°00′30.7″	Gao et al. (2010)
Monzogranite (MG)	421.0 ± 3.7 (MSWD = 0.42, n = 16)	A	Zircon U–Pb SIMS	N37°58′33.6″ E88°56′35.7″	Li et al. (2012a)
Alkali feldspar granite (AG)	432.3 ± 0.8 (MSWD = 0.50, n = 3)	A	Zircon U–Pb LA-ICP-MS	N37°58′25″ E88°50′30″	Bao et al. (2008) Li et al. (2013)
Alkali feldspar granite (AG)	430.5 ± 1.2 (MSWD = 0.01, n = 30)	A	Zircon U–Pb LA-ICP-MS	N37°58′38.6″ E88°55′38.9″	Gao and Li (2011)
Alkali feldspar granite (AG)	422.0 ± 3.0 (MSWD = 2.4, n = 16)	A	Zircon U–Pb SIMS	N37°58′27.6″ E88°56′35.0″	Li et al. (2012a)
Syenogranite (SG)	428.2 ± 4.2 (MSWD = 3.4, n = 16)	S	Zircon U–Pb LA-ICP-MS	N37°56′18″ E88°54′21″	Wang et al. (2014b) and this study
Syenogranite (SG)	422.5 ± 2.3 (MSWD = 1.4, n = 19)	S	Zircon U–Pb LA-ICP-MS	N37°55′24″ E88°52′44″	Wang et al. (2014b)
Granite (Syenogranite?) responsible for the W–Sn mineralization	416.9 ± 2.9	S?	Zircon U–Pb SHRIMP	In Kekekaerde deposit	Sun et al. (2009)
Syenogranite responsible for the W–Sn mineralization (SG)	413.6 ± 2.4 (MSWD = 0.36, n = 30)	S	Zircon U–Pb LA-ICP-MS	N37°56′13″ E88°54′44″	This study
W–Sn mineralization ages					
Strongly greisenized syenogranite responsible for the W–Sn mineralization	411.7 ± 2.6 (MSWD = 0.21, n = 8)	–	Muscovite Ar–Ar	N37°57′30″ E88°56′23″	This study
Wolframite-bearing quartz vein associated with muscovite	412.8 ± 2.4 (MSWD = 0.22, n = 10)	–	Muscovite Ar–Ar	N37°57′36″ E88°56′24″	This study
Wolframite-bearing quartz vein associated with muscovite	413.8 ± 2.6 (MSWD = 0.46, n = 9)	–	Muscovite Ar–Ar	N37°57′28″ E88°56′26″	This study

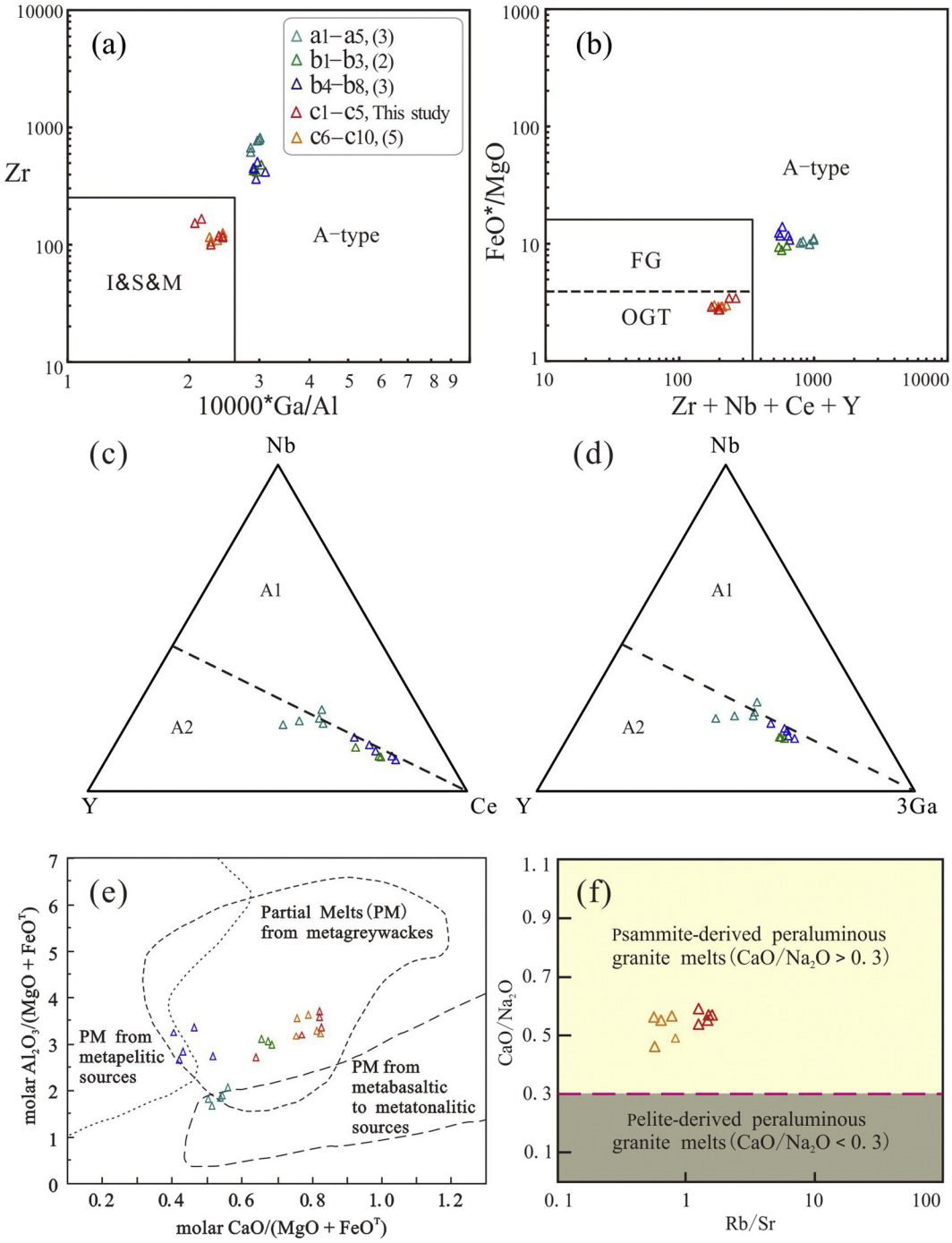

Fig. 14. (a) and (b) Genetic discrimination diagrams for the granitoids in the Bashierxi magmatic series (after Whalen et al., 1987). (c) and (d) Discrimination diagrams for the A-type granites in the Bashierxi magmatic series (Eby, 1992). (e) and (f) Discrimination diagrams for the source rocks of the granitoids in the Bashierxi magmatic series (after Altherr et al., 2000 and Sylvester, 1998, respectively). Symbols and references are the same as those in Fig. 2.

field. Consequently, we believe that the syenogranites show an S-type affiliation.

On the other hand, the monzogranites and alkali feldspar granites (samples a1–a5 and b1–b8, respectively) exhibit high alkali contents ($Na_2O + K_2O$ = 8.30–9.69%), elevated $FeO^T/(FeO^T + MgO)$ ratios (0.90–0.93) and 10,000 × Ga/Al ratios (2.85–3.10), as well as high concentrations of Zr, Nb, Ce, and Y, with Σ(Ce + Zr + Y + Nb) = 556–1006 ppm (Table 3), and thus show geochemical features typical of A-type granites (Loiselle and Wones, 1979; Collins et al., 1982; Whalen et al., 1987; Eby, 1992; Frost et al., 2001; Bonin, 2007). The geochemical affinity of the monzogranites and alkali feldspar granites to A-type granites is also further supported by their exclusive distribution in the A-type granite field on the discrimination diagrams of Whalen et al. (1987) (Fig. 14a,b). Moreover, zircon saturation temperatures in the monzogranites and alkali feldspar granites (averages of 905 °C and 873 °C, respectively; Table 3) are generally consistent with the zircon saturation temperatures in A-type granites in the Paleozoic Lachlan Fold Belt of southeastern Australia (840 °C–900 °C, King et al., 1997, 2001). However, these saturation temperatures are much higher than the maximum crystallization temperatures of the syenogranites (751

Table 3
Main geochemical characteristics and parameters of the granitoids the Bashierxi magmatic series.

Lithology	Syenogranite (SG)			Alkali feldspar granite (AG)		Monzogranite (MG)
	Fresh	Fresh	Strongly greisenized	Fresh	Fresh	Fresh
Sample number	c1–c5	c6–c10	c0	b1–b3	b4–b8	a1–a5
Zr (ppm)	100–168 (131)	107–126 (116)	141	416–478 (441)	359–506 (436)	624–812 (736)
Nb (ppm)	14–17 (16)	12–16 (14)	8	17–18 (18)	16–26 (21)	35–46 (41)
Ce (ppm)	41–51 (45)	43–57 (51)	23	84–123 (108)	81–182 (122)	84–94 (89)
Y (ppm)	20–27 (23)	22–28 (24)	10	29–30 (30)	23–35 (29)	46–87 (59)
10,000*Ga / Al	2.08–2.43 (2.26)	2.25–2.44 (2.35)	3.21	2.89–3.03 (2.96)	2.89–3.10 (2.96)	2.85–3.01 (2.93)
Ce + Zr + Y + Nb (ppm)	176–263 (214)	184–225 (205)	182	562–645 (598)	556–666 (607)	797–1006 (924)
K_2O (%)	3.54–4.23 (3.91)	2.88–4.13 (3.60)	2.66	5.44–6.24 (5.80)	5.25–5.56 (5.42)	5.81–6.29 (6.02)
$K_2O + Na_2O$ (%)	6.86–7.56 (7.28)	6.79–7.61 (7.32)	2.93	8.30–8.54 (8.49)	8.59–9.38 (9.01)	9.54–9.69 (9.59)
$FeO^T/(FeO^T + MgO)$	0.73–0.78 (0.75)	0.74–0.75 (0.75)	0.76	0.90–0.91 (0.91)	0.91–0.93 (0.92)	0.91–0.92 (0.91)
A/CNK	1.07–1.11 (1.09)	1.08–1.12 (1.09)	2.23	0.95–0.97 (0.96)	0.99–1.02 (1.01)	0.92–0.94 (0.93)
TREE (ppm)	103–128 (113)	109–141 (126)	56	203–279 (251)	200–413 (283)	224–306 (248)
LREE/HREE	5.86–6.37 (6.12)	6.69–7.47 (7.13)	7.24	8.41–11.11 (10.19)	8.41–14.06 (11.38)	3.75–6.06 (5.23)
δEu	0.41–0.56 (0.47)	0.42–0.50 (0.46)	0.29	0.71–0.84 (0.77)	0.58–0.85 (0.73)	0.50–0.94 (0.81)
Rb (ppm)	250–305 (267)	172–226 (194)	272	111–115 (113)	100–121 (111)	119–149 (135)
Sr (ppm)	159–244 (193)	250–319 (292)	23	85–86 (86)	81–93 (87)	137–156 (145)
Ba (ppm)	283–376 (312)	289–351 (323)	177	799–845 (822)	777–919 (837)	1259–1397 (1349)
K/Rb	115–130 (122)	134–170 (154)	81	389–408 (399)	410–471 (434)	324–424 (373)
Nb/Ta	3–6 (4)	5–7 (6)	6	14–18 (17)	18–21 (19)	16–21 (19)
Zr/Hf	28–30 (29)	29–36 (34)	31	43–44 (44)	40–41 (41)	43–45 (44)
Crystallization age (Ma)	413.6 ± 2.4	422.5 ± 2.3 428.2 ± 4.2	–	430.5 ± 1.2	432.3 ± 0.8 422.0 ± 3.0	458.0 ± 9.0 (?) 421.0 ± 3.7
T_{Zr}	751–791 °C (771 °C)	755–767 °C (761 °C)	–	866–880 °C (871 °C)	857–887 °C (875 °C)	891–917 °C (905 °C)
Genetic type	S	S	S	A	A	A
Data source	This study	Wang et al. (2014b)	This study	Gao and Li (2011)	Bao et al. (2008); Li et al. (2012a)	Gao et al. (2010); Li et al. (2012a)

Notes: Data in parentheses are the average values. Values of trace elements have been rounded. Symbols in the first column are the same in Table 1.

°C for samples c1–c10; Table 3), which were inferred from the lower limits of calculated zircon saturation temperatures, as some zircons in the samples are inherited.

The monzogranites contain hornblende (ferro-pargasite of calcium amphiboles) that has penetrated the interstices between feldspar and quartz, both of magmatic origin (Fig. 3b), and locally even includes magmatic quartz (Fig. 3b), indicating that the hornblende crystallized later than, or nearly contemporaneously with, the feldspar and quartz; such petrographic features are common in A-type granites. In terms of the chemistry of the hornblende, even though sodic amphibole appears to be dominant in many A-type granites (Wang et al., 2001; Ogunleye et al., 2005; Kynicky et al., 2011), calcic amphibole has also been reported (Han et al., 1997; Dall' Agnol et al., 1999a; Wu et al., 2002).

Interestingly, the rock assemblages and whole-rock geochemistry, as well as the mineralogy of the monzogranite and the alkali feldspar granite in the Bashierxi magmatic series, are surprisingly similar to those of A-type monzogranites and alkali feldspar granites of the Xiaocaohu pluton in North Xinjiang, China (Han et al., 1997). All the above features indicate that the monzogranite and the alkali feldspar granite cropping out in the northeast part of the orefield are A-type granites.

5.3. Geodynamic setting of the Bashierxi magmatic series

As discussed above, the Bashierxi magmatic series was emplaced mainly at ca. 432–413 Ma, with a nearly contemporaneous evolution from A-type granites (monzogranites and alkali feldspar granites, ~432–421 Ma) to S-type granites (syenogranites, ~428–413 Ma). Furthermore, considering that the A- and S-type granites were emplaced in close proximity to one another in this area, and that both intruded the Xiaomiao Formation of the Paleoproterozoic Jinshuikou Group (Fig. 2), we infer that the A- and S-type granites were emplaced in basically the same tectonic setting.

On the basis of trace-element geochemical variations, Eby (1992) sub-divided A-type granites into two groups: (1) an A1 group, with Y/Nb < 1.2, derived from the mantle and emplaced in anorogenic settings, such as in continental rifts or other intraplate environments; and (2) an A2 group, with Y/Nb > 1.2, derived from the melting of continental crust or underplated crust, and emplaced in a variety of tectonic settings. Bonin (2007) reviewed this two-fold subdivision of A-type granites and pointed out that the dataset used by Eby did not show evidence of two discrete groups, but rather illustrated a

continuous shift from post-collision A2 to postorogenic (straddling the A1–A2 boundary) to within-plate A1 suites. All samples of A-type granites from the Bashierxi magmatic series show Y/Nb ratios slightly greater than 1.2, and approach the A1–A2 boundary on Nb–Y–Ce and Nb–Y–3*Ga triangular diagrams (Fig. 14c,d), which indicates that these A-type granites were probably emplaced in a post-orogenic tectonic setting.

Based on mineralogy and major-element chemistry, Maniar and Piccoli (1989) categorized granitoids by tectonic environment as orogenic or anorogenic. Post-orogenic granitoids (POGs) are included in the former, while rift-related granitoids (RRGs) are included in the latter. The mineral assemblages that distinguish POGs and RRGs are the assemblages (biotite ± hornblende) or (biotite ± muscovite), which typify assemblages in POGs, and the assemblage (alkali amphibole ± biotite ± hornblende ± pyroxene) or (biotite ± hornblende ± pyroxene), which typify assemblages in RRGs (Maniar and Piccoli, 1989). The A- and S-type granites of the Bashierxi magmatic series possess the characteristic mineral assemblages (biotite ± hornblende) and (biotite + muscovite) (Fig. 3), which are similar to those of POGs. The compositions of the hornblendes in the granites (calcium amphibole rather than alkali amphibole), as well as the anhedral shape of the hornblende and biotite grains in these characteristically pink–red A-type granites, also suggest that they belong to POGs rather than RRGs, as suggested by Bonin (2007, pages 5, 14) for the recognition of post-orogenic igneous suites.

A comparison of the studied granites with those in true anorogenic settings, such as the Younger Granites of Nigeria, which represent episodically migrating mid-plate magmatism (Bowden and Kinnaird, 1984; Obaje, 2009), reveals a variety of differences. In the field, the Younger Granites occur mainly in the form of ring complexes accompanied by congenetic volcanos (Bowden and Kinnaird, 1984; Mücke, 2003), which are distinguished from the NE-trending linear distribution of the Bashierxi magmatic series along the Baiganhu Fault (Figs. 1, 2). Geochemically and mineralogically, the Younger Granites are generally peralkaline, apart from the calcium amphibole, sodic amphiboles like arfvedsonite and riebeckite, and with alkaline pyroxenes like aegerines, which are common; see "Peculiarities of the Younger Granites" (Obaje, 2009, page 39). The Younger Granites also contain highly Fe-rich minerals, such as nearly pure fayalite, hedenbergite, and Fe-rich augite (Mücke, 2003), which are hardly observed in the Bashierxi magmatic series. In addition, on an A1–A2 discrimination diagram for A-type granites (Eby, 1992), all samples from the Younger Granites fall into the A1 granite field (Dall' Agnol et al., 1999b, see their Fig. 11). These differences show that the granitoids of the Bashierxi magmatic series probably do not belong to anorogenic granites.

More recently, geodynamic studies in the Baiganhu and adjacent region (Liu et al., 2013 and references therein; Wang et al., 2014a) suggest that the ca. 504–486 Ma high-pressure/ultra-high-pressure metamorphic rocks, and voluminous and discrete ca. 485–440 Ma post-collisional to ca. 440–380 Ma post-orogenic magmatic suites, as well as Ordovician–Silurian extensional basins distributed within the South Altyn–Qimantagh, correspond to collisional orogenesis and extensional collapse along the Altyn Tagh–East Kunlun during the Paleozoic.

Taking all of the above observations into consideration, we favor the hypothesis that the ca. 432–413 Ma Bashierxi magmatic series was emplaced in a post-orogenic setting.

5.4. Possible magmas sources for the Bashierxi magmatic series

Although the REE patterns of the S-type granites (c1–c10) in the Bashierxi magmatic series are generally parallel to those of the A-type granites (a1–a5 and b1–b8), the major and trace element variations (Fig. 11) and the peak $\varepsilon_{Hf}(t)$ values of the S-type granites differ between the two types (Fig. 13), suggesting they were probably derived from different sources. This suggestion is slightly different from the conclusions of a recent report that A- and S-type granites in the Krušné Hory/Erzgebirge Mountains of Central Europe are nearly contemporaneous (330–295 Ma); however, in this instance, the εNd values of the two magma suites are very similar, and thus it was envisaged that both types of magma originated through melting of a similar protolith (Breiter, 2012).

The S-type granites in the Bashierxi magmatic series exhibit marked enrichment in some large-ion lithophile elements (LILEs) (e.g., Rb and K) and depletion in high-field-strength elements (HFSEs) (e.g., Nb, Ta, and Ti), which is consistent with the involvement of crustal components (Taylor and McLennan, 1995). Furthermore, these syenogranites yield zircon U–Pb age of 413.6 ± 2.4 Ma and exhibit negative zircon $\varepsilon_{Hf}(t)$ values of −8.5 to −1.1 (average, −3.8; Fig. 13c) with two-stages Hf model ages (T^{C}_{DM}) of 1467–1931 Ma (age peak at 1550–1700 Ma; Fig. 13d). This latter age range corresponds to that of crystalline basement in the Jinshuikou Group, in a region where the rocks are mainly of late Paleoproterozoic age (Mo et al., 2007 and references therein). In addition, the S-type granites show corresponding high molar ratios of $CaO/(MgO + FeO^{T})$, $Al_2O_3/(MgO + FeO^{T})$, and CaO/Na_2O, suggesting a metapsammite (or metagreywacke) source (Fig. 14e,f), which is also compatible with the major lithologies in the upper Jinshuikou Group (Ding, 2004). Consequently, we propose that the parental magma of the S-type granites likely originated by partial melting of the Paleoproterozoic Jinshuikou Group.

The A-type alkali feldspar granites in the Bashierxi magmatic series yield an U–Pb zircon age of ~430.5 Ma (b1–b3, Gao and Li, 2011) and show zircon $\varepsilon_{Hf}(t)$ values of −2.3 to +5.6 (average, +1.5; Fig. 13c), with younger two-stage Hf model ages (T^{C}_{DM}) of 1059–1556 Ma (age peak at 1250–1400 Ma; Fig. 13d), suggesting that the parental magma also originated from partial melting of old crustal components, but involved certain contributions of new crustal material. Samples of the A-type monzogranites (a1–a5) and the alkali feldspar granites (b1–b3, b4–b8) in the Bashierxi magmatic series show variable values of molar $Al_2O_3/(MgO + FeO^{T})$ and $CaO/(MgO + FeO^{T})$ ratios, which group into metagreywacke, metapelite, or metabasalt–metatonalite sources (Fig. 14e), and which are also compatible with the considerable variety of lithologies observed in the lower Jinshuikou Group, especially those of the Baishahe Formation (Ding, 2004; Lei et al., 2010). Previous research has shown that the K_2O content of magma is controlled mainly by pressure conditions (Defant and Drummond, 1990; Ellam, 1992; Skjerlie and Johnston, 1996; Wang et al., 2007), and Wang et al. (2008) recently proposed a rough positive correlation between the K_2O content of granitoids and the depth of the parental magma. The K_2O contents of the A-type granites in the Bashierxi magmatic series (a1–a5, b1–b8) (5.25%–6.29%; average, 5.80%) are higher than those of the S-type granites (c1–c10) (2.88%–4.23%; average, 3.75%), which implies that the magma source of the A-type granites was likely deeper than that of the S-type granites, thus confirming speculations regarding the source depths of the magmas yielding the S-type and A-type granites (see above). Thus, we argue that the A- and S-type granites likely originated, at least to a certain extent, from the partial melting of various discrete components of the Paleoproterozoic Jinshuikou Group, corresponding to different depths of burial, despite the fact that the A-type granites probably involved components of certain new crustal materials.

5.5. Relationship between rocks in the Bashierxi magmatic series and W–Sn mineralization

The muscovite ^{40}Ar–^{39}Ar dating method has proven powerful for obtaining precise ages of ore deposits (Feng et al., 2015 and references therein). Our ^{40}Ar–^{39}Ar ages for hydrothermal muscovite in the Kekekaerde deposits show well-defined weighted plateau ages of 411.7 ± 2.6 Ma, 412.8 ± 2.4 Ma, and 413.8 ± 2.6 Ma which are the same within error, and which are consistent with corresponding $^{39}Ar/^{36}Ar$–$^{40}Ar/^{36}Ar$ isochron ages of 411.8 ± 4.7 Ma, 414.6 ± 3.9 Ma, and 414.0 ± 4.0 Ma. These data indicate that the W–Sn mineralization

in the Kekekaerde deposit occurred mainly in the beginning of the Early Devonian, corresponding to the late stage of the Caledonian Cycle.

The W–Sn mineralization ages obtained from the Kekekaerde deposit are also considered to roughly represent the ages of samples in the Baiganhu deposit, as the Baiganhu and Kekekaerde deposits are in close proximity (Figs. 1, 2), and both share the three types of W–Sn mineralization and related alteration (Figs. 5–7). Thus, the mineralization ages of 411.7 ± 2.6 Ma, 412.8 ± 2.4 Ma, and 413.8 ± 2.6 Ma, which are in agreement with the crystallization age of 413.6 ± 2.4 Ma for the parental syenogranite, indicate a temporal link between the syenogranite and the W–Sn mineralization. Moreover, as mentioned above, the chemical features of the magmatic garnet (almandine–spessartine series) and biotite (relatively rich in Fe) in the syenogranites are shared by those of the parental granites, such as in the Xihuashan Sn deposit and the recently discovered Dahutang W deposit (Yang et al., 2013; Huang and Jiang, 2014). And most of all, as detailed above, the syenogranites show a close spatial association with the W–Sn mineralization, and the three types of mineralization show an outward zonation from the syenogranite intrusions (Figs. 5–7). All of these observations indicate that the syenogranites of S-type affiliation in the Bashierxi magmatic series are spatially and temporally associated with the W–Sn mineralization.

The monzogranites and alkali feldspar granites with A-type affiliations crop out mainly in the northern part of the orefield (Figs. 1, 2), and our detailed field work has shown that rare W–Sn mineralization and accompanying alteration have been discovered in their vicinity. The question thus arises as to why the syenogranites of S-type affiliation are more closely related to W–Sn mineralization than the nearby monzogranites and alkali feldspar granites of A-type affiliation. Four main factors, among others, have been considered in relation to this question, as follows.

The first factor is related to magma sources. The concentration of mineral deposits in magma in the context of a magmatic hydrothermal paradigm has been substantiated in numerous studies on geological field relations, fluid inclusions, and isotopic geochemistry (Ishihara, 1977; Candela and Bouton, 1990; Linnen and Cuney, 2005; Maulana et al., 2013). The W–Sn mineralization system in the Baiganhu orefield also conforms to this paradigm, based on the aforementioned detailed description of alteration and mineralization, and on the H–O isotopic data, which reveal that the hydrothermal fluid evolved from a fluid of mainly magmatic origin to a fluid dominated by mixed meteoric and metamorphic water (Li et al., 2012b; Feng et al., 2013). As mentioned above, geochemical and Hf isotopic data suggest that the S-type granites in the Bashierxi magmatic series were derived mainly from a metagreywacke source, while metabasalt–metatonalite and young crustal materials (in addition to the metagreywackes and metapelite) probably contributed to the formation of the A-type granites. Differences in source lithologies and related elemental abundances probably led to at least two significant variations in the subsequent partial melt, related to (i) the concentration of ore-forming elements such as W and Sn, and (ii) the contents of volatiles, such as boron and water.

The W abundance in various igneous, sedimentary, and metamorphic rocks in the lithosphere around the world has been summarized by Liu and Ma (1987). Accordingly, the average content of W in sandstones and pelitic rocks, as well as in related low- to medium-grade metamorphic rocks, is much higher than that in ultramafic, mafic, and intermediate rocks, such as peridotite, basalt, and diorite. The analogous trends for W and Sn were also determined by Yan and Chi (1997) and Chi et al. (2012), by analyzing and summarizing the large amounts of geochemical data of various rocks in eastern China, including in the Inner Mongolia–Jihei Orogenic Belt, North China Craton, Qinling–Dabie Orogenic Belt, Yangtze Block, and Cathaysia Block. Chi et al. (2012) also considered that the source rocks of the magma–the Mesoproterozoic metasandstones and metamudstones which are rich in tungsten and tin–exert a strong positive influence on the large numbers of magmatic–hydrothermal W–Sn deposits in South China.

The development of abundant tourmalines in the Baiganhu W–Sn orefield, especially in greisenized and scheelite-mineralized syenogranite of S-type affiliations, shows that boron of mainly magmatic origin plays an important role in W–Sn mineralization. However, the occurrence of tourmaline in the studied A-type granites is rare. Yan and Chi (1997) also pointed out that, unlike fluorine, boron is relatively depleted in ultramafic, mafic, and intermediate rocks, as well as in related metamorphic rocks, with average abundances being generally <10 ppm, but that boron is considerably enriched in greywackes and pelitic rocks, which generally show abundances of >25–75 ppm. Thus, the boron-poor source rocks of the A-type granites probably resulted in a boron-depleted magma, which does not favor the hypothesis of late- to post-magmatic W–Sn mineralization in the Baiganhu orefield.

The water contents of the magmas are relevant to their mode of formation. The letter 'A' in the term 'A-type' granites designates that the rocks crystallized under relatively anhydrous conditions (Loiselle and Wones, 1979). It has also been noted that A-type magmas yield the lowest water fugacities recorded in the realm of silicate magmas (Bonin, 2007), which may also explain why not a few of A-type granites are not related to hydrothermal deposits, except in cases of highly evolved magma (such as in highly evolved peraluminous A-type granites, which are sufficiently rich in F to yield topaz as a rock-forming mineral; Bonin, 2007). The petrographic differences between S- and A-type granites in the Bashierxi magmatic series also show that water concentrations in A-type magmas are lower than those in S-type magmas, as evidenced by the crystallization sequence of water-bearing mafic minerals, such as biotite and/or hornblende, which crystallized later than or nearly contemporaneously with the felsic minerals in the A-type granites, but earlier in the S-type granites (Fig. 3). In addition, the S-type granites contain primary muscovite and belong to muscovite-bearing granitoids (MPG-type), usually on account of the 'wet' anatexis of crustal rocks (Barbarin, 1999).

Based on the observations above, we infer that the various protoliths of the S- and A-type granites, which resulted in different concentrations of elements and compounds in the magma (such as W, Sn, B, and H_2O), were to a large extent be responsible for mineralization disparity during late- to post-magmatic evolutionary processes, although such imparities are not observable in the actual source rocks at present exploration levels.

A second factor that contributes to the pattern of syenogranites of S-type affiliation being more closely related to W–Sn mineralization than nearby monzogranites and alkali feldspar granites of A-type affiliation is *the degree of partial melting*. The scarcer occurrences (or absence) of inherited zircons in A-type granites than in S-type granites suggests that the A-type granites resulted from a higher degree of partial melting, which is also demonstrated by zircon saturation temperatures (T_{Zr}), which are much higher in the A-type granites ('hot' granitoids) than in the S-type granites ('cold' granitoids). Although the effects of partial melting have often been ignored or considered insignificant, higher degrees of partial melting actually do not favor the further enrichment of incompatible lithophile elements such as W, Sn and B in melts (Liu et al., 1984; Liu and Ma, 1987). In the Bashierxi magmatic series, the S-type syenogranites resulted from a lower degree of partial melting, and are more likely to be associated with post-magmatic W–Sn mineralization than are A-type syenogranites.

The third factor in the observed preferential affiliation of W–Sn mineralization with S-type granites is *the degree of crystallization differentiation*. Fractional crystallization leads to enrichment of W–Sn in magma (Liu and Ma, 1987; Huang and Jiang, 2014 and references therein). This differentiation process has been described for granites of the Jalama batholith, Portugal (Ruiz et al., 2008), in S-type granitic rocks of northern and central Portugal (Neiva, 2002), and in some granites of the Krušné Hory/Erzgebirge Mountains in Central Europe (Breiter, 2012). As mentioned above, although the S- and A-type granites in the Bashierxi magmatic series were probably derived from different sources, the much lower values of K/Rb, Nb/Ta, Zr/Hf, and Ba, together

with the lower TREE contents (especially LREE contents) and stronger negative Eu anomalies in the S-type granites as compare with the A-type granites (Fig. 11, Table 3), suggest that a higher degree of fractional crystallization in the S-type granites is likely (Whalen et al., 1987; King et al., 2001; Hua et al., 2007; Huang and Jiang, 2014); the higher degree of fractional crystallization also favors late- to post-magmatic W–Sn mineralization.

The last factor to consider in the preferential affiliation of W–Sn mineralization with S-type granites is *the oxidation state*. Tungsten and Sn mineralization tends to form in reduced granitic magmas typically belonging to the ilmenite series (Ishihara, 1977, 1981, 2004). The Fe^{3+}/Fe^{2+} ratios in S-type granitoids in the Bashierxi magmatic series are in the range of 0.19–0.46 (average, 0.30) (Table 1), which, based on available data, is lower than that of A-type granites, which are in the range of 0.50–0.56 (average, 0.52) (Gao and Li, 2011). When plotted on a redox state discrimination diagram for igneous rocks (Blevin, 2004), almost all of the S-type samples fall into the moderately reduced field (MR), under but close to the fayalite–magnetite–quartz buffer (FMQ) field, whereas all of the A-type samples fall into the moderately oxidized (MO) field, between the titanite–magnetite–quartz–hedenbergite–ilmenite (TMQHIL) and FMQ buffer fields. In fact, it has been noted that S-type granites are invariably reduced (Blevin and Chappell, 1995) whereas A-type granites in late orogenic environments belong to the magnetite series (Ishihara, 2004), which is relatively oxidized.

In the case of magnetite-series granites (characterized by higher Fe^{3+}/Fe^{2+} ratios), as proposed by Ishihara (1977, 1981), *tin* is in the tetravalent state (Sn^{4+}), and as such may substitute for Ti or Fe, thus entering the lattice of early crystallizing rock-forming minerals such as sphene, magnetite, hornblende, and biotite. The availability of Sn in the remaining liquid fraction would hence be limited, with the further consequence that accumulation of Sn in the residual melt would be insufficient to produce an ore deposit. This is probably not the case for A-type granites in the Bashierxi magmatic series, as the mafic minerals in these rocks mostly crystallized later. However, in the case of ilmenite-series granites (with lower Fe^{3+}/Fe^{2+} ratios), Sn is in the divalent state (Sn^{2+}), and as such cannot enter the lattice of early forming minerals. Under these conditions, Sn is more readily available to accumulate in residual melts, leading to Sn-rich and highly fractionated granites (Pirajno, 2009, page 228). This may explain the reduced S-type granites associated with W–Sn mineralization in the Baiganhu orefield.

The effect of oxidation state on the concentration of *tungsten* in the course of magmatic and hydrothermal evolution is somewhat more complex. Tungsten dissolves predominantly as W^{6+} at all oxygen fugacities above an iron–wüstite (IW) buffer value of −3.6 in silicate magma, and W^{4+} may contribute W only at the very lowest oxygen fugacity levels, as confirmed by experiments using silicate melts (Wade et al., 2013 and references therein). Given that the oxygen fugacity of the studied S- and A-type granites is higher than the IW buffer value of −3.6, the valence state of W in both the S- and A-type magmas is likely to be hexavalent, which is independent of oxygen fugacity. It has also been noted that, in an early stage of granitic magma evolution, fractional crystallization processes would be more dominant in controlling the concentration of W, rather than the oxidation state (Huang and Jiang, 2014 and references therein). However, during the late stages of magmatic evolution, the oxygen fugacity can influence the relative efficiency of the release of W from magma into hydrothermal ore-forming fluids (Huang and Jiang, 2014), as demonstrated by experiments on W to determine fluid/mineral partition coefficients (Candela and Bouton, 1990; Bali et al., 2012); these experiments have shown that conditions of low oxygen fugacity can promote the accumulation of W in hydrothermal fluids. In addition, Ague and Brimhall (1988) identified conditions for the formation of W-rich deposits in which the oxygen fugacity is below the value of the QFM buffer.

The studied S-type granites have oxygen fugacities below the QFM buffer, which can result in the release substantial amounts of W from the magma to hydrothermal fluids. On the other hand, the A-type granites show higher oxygen fugacities, thus promoting conditions that can retain W in the rock-forming minerals in the late stages of the evolution of the granitic magma, thus against forming an economically significant tungsten deposit.

Consideration of these factors indicates a sound basis for the preferred association of S-type syenogranites with W–Sn mineralization in the Bashierxi magmatic series, as compared with the association of mineralization and A-type monzogranites and alkali feldspar granites, although the mechanisms controlling the concentration of W and Sn in the different rocks vary according to the four factors discussed above. Overall, our detailed field work, together with the geochemical and geochronological data, lead us to conclude that the syenogranites of S-type affiliation are more closely associated with W–Sn mineralization than are the monzogranites and alkali feldspar granites of A-type affiliation. Notably, among the various arguments presented for this preferential association, the most important are the systematic field observations of the mineralization and its related alteration, as presented in detail in the previous sections. Consequently, we suggest that more attention should be given to buried and apophysis-bearing syenogranites of S-type affinity during exploration for W–Sn resources in the Baiganhu and adjacent area, as the major W–Sn orebodies that meet this condition occur mainly in the exogranite and in the upper portions of the cupola, which have experienced little erosion.

5.6. An alternative petrogenetic and metallogenic model for the Bashierxi magmatic series

Occurrences of nearly contemporaneous A- and S-type granites are rare (Breiter, 2012), as are petrogenetic models for their association, which is probably related to the fact that many A-type granites formed in extensional tectonic settings whereas most S-type granites formed in collisional tectonic environments. Based on field and petrologic evidence (Figs. 1, 2), together with age data, and whole-rock geochemical and isotopic data (Figs. 11, 13), we developed a simple and tentative model explaining the presence of both A- and S-type granites in the Bashierxi magmatic series, on the basis of the new model for A-type granitoids (Azzouni-Sekkal et al., 2003; Liégeois et al., 2005; Bonin, 2007).

As discussed above, the A- and S-type granites in the Bashierxi magmatic series were likely emplaced in a post-orogenic setting, following the amalgamation of East Kunlun and Altyn Tagh. According to a more detailed analysis of the stages of the Wilson orogenic cycle, A-type granites during the post-collision orogenic stage are considered to be emplaced in transcurrent shear zones (Bonin, 2007), such as in the "Taourirt" magmatic province in Hoggar, Algeria (Azzouni-Sekkal et al., 2003). Lithospheric control by large-scale shear zones is evidenced by long-lasting fluid percolation, alteration of primary rock compositions, perturbation of isotopic signatures (e.g., Azzouni-Sekkal et al., 2003), and associated concentrations of economically important minerals, such as W–Sn–Mo, Au, Nb–Ta, and Th–U (Bonin, 2007).

Following the model proposed by Liégeois et al. (2005) and Liégeois et al. (2013) for the Hoggar volcanism in the central Sahara, we envisage that during the Caledonian post-collisional stage, in the region between the Altyn Tagh and the East Kunlun terranes, major linear delamination induced asthenospheric upwelling that melted the continental crust. The A-type magma is considered to be the result of partial melting of the lower portions of the Paleoproterozoic Jinshuikou Group, involving some amount of new crustal material. On the other hand, partial melting of the upper parts of the Jinshuikou Group gave rise to the formation of S-type magma. It is envisaged that the A-type magma was emplaced and crystallized slightly prior to the S-type syenogranitic magma; thus, the A-type granites show slightly older ages (Fig. 2). However, mixing between the A-type and S-type magmas more or less probably took place during the process of gathering, upwelling, storage, and emplacement, a scenario that may explain the similarity between the REE

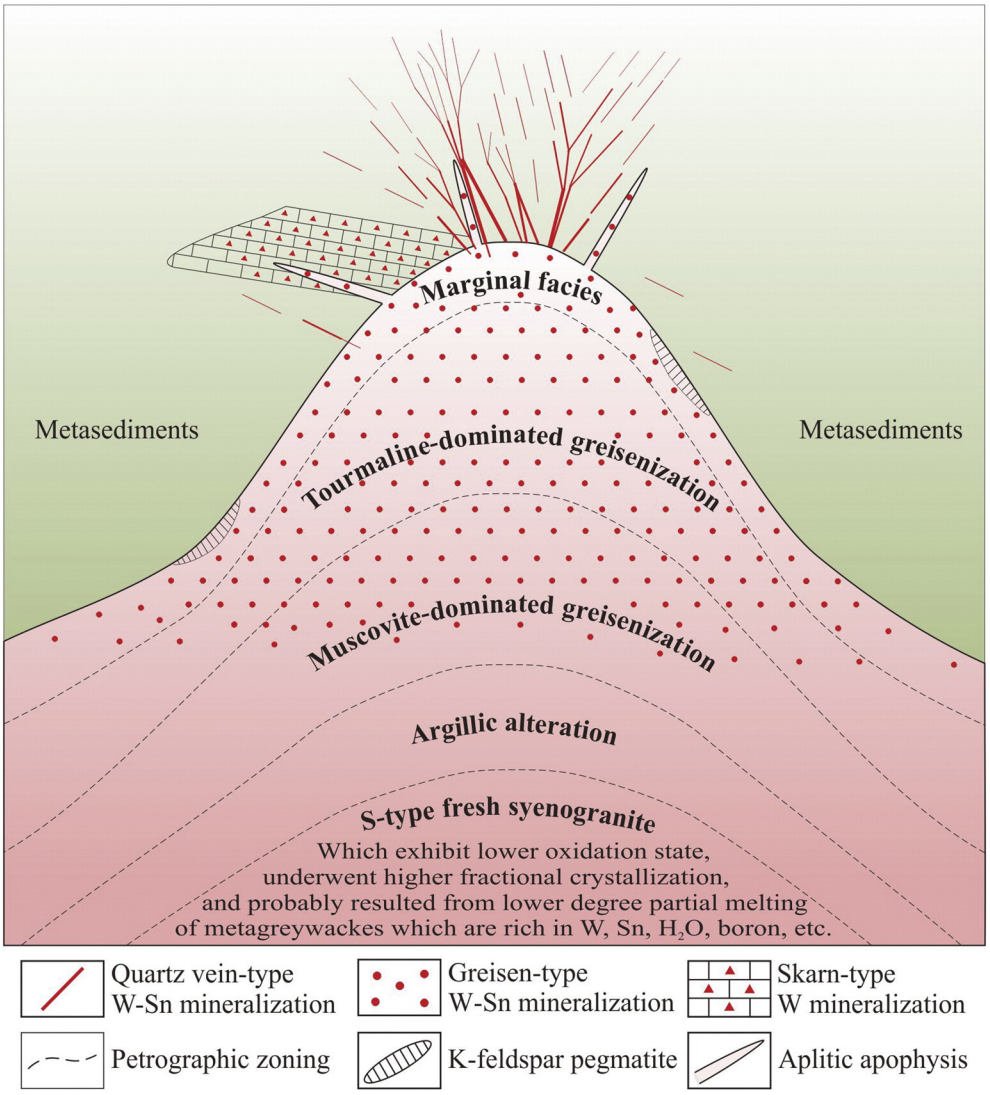

Fig. 15. Proposed genetic model for the Baiganhu W–Sn orefield (see text for details).

patterns in the A- and S-type magmas, but also the difference in $\varepsilon_{Hf}(t)$ values for the two magma types (Figs. 11, 13; Table 3).

As for metallogenic processes, the higher abundances of some elements (such as the ore-forming elements W and Sn, and the volatiles B and H_2O) in the source rocks, and the higher degree of fractional crystallization, together with the lower degree of partial melting and lower oxidation state of the S-type granites, probably resulted in S-type syenogranites that more likely formed post-magmatic W–Sn mineralization. A preliminary metallogenic model for the Baiganhu orefield is shown in Fig. 15. To better understand the ore-forming processes of this outstanding large-scale multi-type Caledonian W–Sn orefield in northwest China, further investigations, including more detailed mineralogical and fluid inclusion studies, are needed in the future.

6. Summary and conclusions

Results of this work indicate that the evolution of the Baiganhu orefield involved three major stages of W–Sn mineralization, occurring at ca. 413–411 Ma; from early to late, the stages are represented by skarn-, greisen-, and quartz-vein-type mineralization.

The greisen-type scheelite mineralization in the orefield is dominated by a B-rich system (abundant in tourmaline and relatively poor in fluorite and topaz), and reverse alteration zoning in the intrusion is considered to exist in these deposits.

We suggest that the Bashierxi magmatic series was emplaced in a post-orogenic setting from the early Silurian to the Early Devonian (~432–413 Ma), and involved nearly contemporaneous emplacement of A- and S-type granites, which are likely the products of partial melting of various continental source components, triggered by major linear delamination and subsequent asthenospheric upwelling.

The syenogranites of S-type affinity in the Bashierxi magmatic series are spatially and temporally associated with the W–Sn mineralization, and probably resulted from a relatively low degree of partial melting of metagreywacke, which is rich in the ore-forming elements W and Sn, as well as the volatiles B and H_2O. In addition, the syenogranites exhibit lower oxidation states and higher degrees of fractional crystallization than the A-type granites. We suggest that more attention should be paid to buried apophysis-bearing syenogranites of S-type affinity during further exploration in the Baiganhu and adjacent area.

Conflict of Interest

No.

Acknowledgments

This study was financially supported by grant No. 41172076 from the National Natural Science Foundation of China and the Program of

High-Level Geological Talents (201309) and Youth Geological Talents (201112) of the China Geological Survey. We thank Anshun Zhou, Shuo Wang, Ye Xiao, Jiannan Liu, and Miao Yu for their help during field work. We also appreciate the assistance of Zhenyu Chen with electron microprobe analyses, Yuejun Deng with whole-rock geochemical analyses, Kejun Hou with LA-ICP-MS U–Pb dating and Lu–Hf isotope analyses, and Yan Zhang and Xinyu Liu with ^{40}Ar–^{39}Ar dating at Chinese Academy of Geological Sciences (CAGS), Beijing, China. We are grateful to Dr. Karel Breiter and an anonymous reviewer for their thoughtful reviews and their constructive and stimulating comments, which helped to significantly improve the manuscript. We also thank the Editor-in-Chief, Franco Pirajno, for providing prompt feedback and information on the status of reviews of our paper, and for his assistance and inspiration during the writing and submission process.

Appendix A. Supplementary data

Supplementary data to this article can be found online at http://dx.doi.org/10.1016/j.oregeorev.2015.12.009.

References

Ague, J.J., Brimhall, G.H., 1988. Magmatic arc asymmetry and distribution of anomalous plutonic belts in the batholiths of California: effects of assimilation, crustal thickness, and depth of crystallization. Geol. Soc. Am. Bull. 100, 912–927.

Altherr, R., Holl, A., Hegner, E., Langer, C., Kreuzer, H., 2000. High-potassium, calc-alkaline I-type plutonism in the European Variscides: Northern Vosges (France) and northern Schwarzwald (Germany). Lithos 50, 51–73.

Azzouni-Sekkal, A., Liégeois, J.P., Bechiri-Benmerzoug, F., Belaidi-Zinet, S., Bonin, B., 2003. The "Taourirt" magmatic province, a marker of the closing stage of the Pan-African orogeny in the Tuareg Shield: review of available data and Sr–Nd isotope evidence. J. Afr. Earth Sci. 37, 331–350.

Bali, E., Keppler, H., Audetat, A., 2012. The mobility of W and Mo in subduction zone fluids and the Mo–W–Th–U systematics of island arc magmas. Earth Planet. Sci. Lett. 351, 195–207.

Bao, Y.F., Liu, Y.J., Wang, X.C., 2008. Relations between Bashienerxi granite, west Dongkunlun and Baiganhu tungsten–tin deposit. Jilin Geol. 27, 56–59 (in Chinese with English abstract).

Barbarin, B., 1999. A review of the relationships between granitoid types, their origins and their geodynamic environments. Lithos 46, 605–626.

Blevin, P.L., 2004. Redox and compositional parameters for interpreting the granitoid metallogeny of eastern Australia: implications for gold-rich ore systems. Resour. Geol. 54, 241–252.

Blevin, P.L., Chappell, B.W., 1995. Chemistry, origin, and evolution of mineralized granites in the Lachlan fold belt, Australia; the metallogeny of I-and S-type granites. Econ. Geol. 90, 1604–1619.

Bonin, B., 2007. A-type granites and related rocks: evolution of a concept, problems and prospects. Lithos 97, 1–29.

Bowden, P., Kinnaird, J.A., 1984. The petrology and geochemistry of alkaline granites from Nigeria. Phys. Earth Planet. Inter. 35, 199–211.

Breiter, K., 2002b. From explosive breccia to unidirectional solidification textures: magmatic evolution of a phosphorus-and fluorine-rich granite system (Podlesí, Krušné hory Mts., Czech Republic). B. Czech Geol. Surv. 77, 67–92.

Breiter, K., 2012. Nearly contemporaneous evolution of the A- and S-type fractionated granites in the Krušné hory/Erzgebirge Mts., Central Europe. Lithos 151, 105–121.

Breiter, K., Frýda1, J., Leichmann, J., 2002a. Phosphorus and rubidium in alkali feldspars: case studies and possible genetic interpretation. B. Czech Geol. Surv. 77, 93–104.

Breiter, K., Müller, A., Leichmann, J., Gabašová, A., 2005. Textural and chemical evolution of a fractionated granitic system: the Podlesí stock, Czech Republic. Lithos 80, 323–345.

Candela, P.A., 1997. A review of shallow, ore-related granites: textures, volatiles, and ore metals. J. Petrol. 38, 1619–1633.

Candela, P.A., Bouton, S.L., 1990. The influence of oxygen fugacity on tungsten and molybdenum partitioning between silicate melts and ilmenite. Econ. Geol. 85, 633–640.

Carlin Jr., J.F., 2014. Tin (advance release), 2012: U.S. Geological Survey Minerals Year Book. pp. 77.0–77.9.

Champion, D.C., Bultitude, R.J., 2013. The geochemical and Sr–Nd isotopic characteristics of Paleozoic fractionated S-types granites of north Queensland: implications for S-type granite petrogenesis. Lithos 162, 37–56.

Chappell, B.W., White, A.J.R., 1992. I- and S-type granites in the Lachlan Fold Belt. Geol. Soc. Am. Spec. Pap. 272, 1–26.

Chappell, B.W., White, A.J.R., 2001. Two contrasting granite types: 25 years later. Aust. J. Earth Sci. 48, 489–499.

Chi, Q.H., Wang, X.Q., Xu, S.F., Zhou, J., Liu, H.L., Liu, D.S., Zhang, B.M., Wang, W., 2012. Temporal and spatial distribution of tungsten and tin in South China Continent. Earth Sci. Front. 19, 70–83 (in Chinese with English abstract).

Collins, W.J., Richards, S.W., 2008. Geodynamic significance of S-type granites in circum-Pacific orogens. Geology 36, 559–562.

Collins, W.J., Beams, S.D., White, A.J.R., Chappell, B.W., 1982. Nature and origin of A-type granites with particular reference to southeastern Australia. Contrib. Mineral. Petrol. 80, 189–200.

Dall' Agnol, R., Scaillet, B., Pichavant, M., 1999a. An experimental study of a lower Proterozoic A-type granite from the eastern Amazonian Craton. Brazil. J. Petrol. 40, 1673–1698.

Dall'Agnol, R., Rämö, O.T., de Magalhães, M.S., Macambira, M.J.B., 1999b. Petrology of the anorogenic, oxidised Jamon and Musa granites, Amazonian Craton: implications for the genesis of Proterozoic A-type granites. Lithos 46, 431–462.

Defant, M.J., Drummond, M.S., 1990. Derivation of some modern arc magmas by melting of young subducted lithosphere. Nature 347, 662–665.

Ding, Q.F., 2004. Metallogenesis and Mineral Resources Assessment in Eastern Kunlun Orogenic Belt. Jilin University, Jilin (unpublished Ph.D. thesis). (in Chinese with English abstract).

Eby, G.N., 1992. Chemical subdivision of the A-type granitoids: petrogenetic and tectonic implications. Geology 20, 641–644.

Ellam, R.M., 1992. Lithospheric thickness as a control on basalt geochemistry. Geology 20, 153–156.

Feng, C.Y., Yu, M., Li, D.X., Li, G.C., AS Zhou, A.S., Li, X., 2013. Fluid inclusion geochemistry of Bashierxi tungsten–tin deposit in Qimantag area, Xinjiang. Mineral Deposits 32, 20–36 (in Chinese with English abstract).

Feng, C.Y., Zhao, Z., Qu, W.J., Zeng, Z.L., 2015. Temporal consistency between granite evolution and tungsten mineralization in Huamei'ao, southern Jiangxi Province, China: evidence from precise zircon U–Pb, molybdenite Re–Os, and muscovite ^{40}Ar–^{39}Ar isotope geochronology. Ore Geol. Rev. 65, 1005–1020.

Frost, B.R., Barnes, C.G., Collins, W.J., Arculus, R.J., Ellis, D.J., Frost, C.D., 2001. A geochemical classification for granitic rocks. J. Petrol. 42, 2033–2048.

Gao, Y.B., Li, W.Y., 2011. Petrogenesis of granites containing tungsten and tin ores in the Baiganhu deposit, Qimantage, NW China: constraints from petrology, chronology and geochemistry. Geochimica 40, 324–336 (in Chinese with English abstract).

Gao, X.F., Xiao, P.X., Xie, C.R., Fang, L.Y., Guo, L., Xi, R.G., 2010. Zircon LA-ICP-MS U–Pb dating and geological significance of Bashierxi granite in the eastern Kunlun area, China. Geol. Bull. China 29, 1001–1008 (in Chinese with English abstract).

Gao, Y.B., Li, W.Y., Zhang, Z.W., 2011. Fluid inclusions and H–O isotopic compositions of quartz-vein ores in the BaiganhuJialesai W–Sn mineralization belts, Qimantage, NW China. Acta Petrol. Sin. 27, 1829–1839 (in Chinese with English abstract).

Han, B.F., Wang, S., Jahn, B., Hong, D., Kagami, H., Sun, Y., 1997. Depleted-mantle source for the Ulungur River-type granites from north Xinjiang, China: geochemistry and Nd–Sr isotopic evidence, and implications for Phanerozoic crustal growth. Chem. Geol. 138, 135–159.

Hawthorne, F.C., Oberti, R., Harlow, G.E., Maresch, W.V., Martin, R.F., Schumacher, J.C., Welch, M.D., 2012. Nomenclature of the amphibole supergroup. Am. Mineral. 97, 2031–2048.

Hua, R.M., Zhang, W.L., Gu, S.Y., Chen, P.R., 2007. Comparison between REE granite and W–Sn granite in the Nanling region, South China, and their mineralizations. Acta Petrol. Sin. 23, 2321–2328 (in Chinese with English abstract).

Huang, L.C., Jiang, S.Y., 2014. Highly fractionated S-type granites from the giant Dahutang tungsten deposit in Jiangnan Orogen, Southeast China: geochronology, petrogenesis and their relationship with W-mineralization. Lithos 202–203, 207–226.

Ishihara, S., 1977. The magnetite-series and ilmenite-series granitc rocks. Min. Geol. 27, 293–305.

Ishihara, S., 1981. The granitoid series and mineralization. Econ. Geol. 75th Anniv. vol., pp. 458–484

Ishihara, S., 2004. The redox state of granitoids relative to tectonic setting and earth history: the magnetite-ilmenite series 30 years later. Geol. Soc. Am. Spec. Pap. 389, 23–33.

Jilin Geological Survey Institute, 2009. The report of geological features of Baiganhu W–Sn orefield in Ruoqiang County, Xinjiang. Jilin: Geological Survey Institute of Jilin Province, China (unpublished data).

King, P.L., White, A.J.R., Chappell, B.W., Allen, C.M., 1997. Characterization and origin of aluminous A-type granites from the Lachlan Fold Belt, southeastern Australia. J. Petrol. 38, 371–391.

King, P.L., Chappell, B.W., Allen, C.M., White, A.J.R., 2001. Are A-type granites the high-temperature felsic granites? Evidence from fractionated granites of the Wangrah Suite. Aust. J. Earth Sci. 48, 501–514.

Kynicky, J., Chakhmouradian, A., Xu, C., Krmíček, L., Galiová, M., 2011. Distribution and evolution of zirconium mineralization in peralkaline granites and associated pegmatites of the Khan Bogd complex, southern Mongolia. Can. Mineral. 49, 947–965.

Lei, Y.X., Wang, L.S., Li, H.Y., Hang, Y., Duan, X.X., Li, X., 2010. The compostion comparison of Neoarchaeozoic to Paleoproterzoic volcanic rocks and meta-pelitic rocks and their geological significance in Altyn and East Kunlun. Xinjiang Geol. 28, 142–150 (in Chinese with English abstract).

Li, H.M., Shi, Y.D., Liu, Z., Shao, X.J., 2007. Heishan–Qimantage metallogenic belt in the western section of east Kunlun Mountain, Xinjiang: geologic condition for W and Sn metallogenesis and prospecting guide. Geol. Res. 16, 86–90 (in Chinese with English abstract).

Li, G.C., Feng, C.Y., Wang, R.J., Ma, S.C., Li, H.M., Zhou, A.S., 2012a. SIMS zircon U–Pb age, petrochemistry and tectonic implications of granitoids in northeastern Baiganhu W–Sn orefield, Xinjiang. Acta Geosci. Sin. 33, 216–226 (in Chinese with English abstract).

Li, G.C., Feng, C.Y., Wang, R.J., Li, H.M., Zhou, A.S., Ma, S.C., Liu, J.N., Xiao, Y., 2012b. Study of geological characteristics and fluid inclusions of the Kekekaerde W–Sn deposit in Ruoqiang County, Xinjiang. Acta Geol. Sin. 86, 210–218 (in Chinese with English abstract).

Li, D.P., Li, X.L., Wang, X.L., 2013. Report of Regional Geological Survey (1:250,000 Ayaqikemuhu Area J45C003004). China University of Geosciences Press, Beijing (in Chinese with English abstract).

Liégeois, J.P., Benhallou, A., Azzouni–Sekkal, A., Yahiaoui, R., Bonin, B., 2005. The Hoggar swell and volcanism, Tuareg shield, Central Sahara: intraplate reactivation of Precambrian structures as a result of Alpine convergence. In: Foulger, G.R., Natland, J.H., Presnall, D.C., Anderson, D.L. (Eds.), Plates. Plumes and Paradigms. Geol. Soc. Am. Special Paper 388, pp. 379–400.
Liégeois, J.P., Abdelsalam, M.G., Ennih, N., Ouabadi, A., 2013. Metacraton: nature, genesis and behavior. Gondwana Res. 23, 220–237.
Linnen, R.L., Cuney, M., 2005. Granite-related rare-element deposits and experimental constraints on Ta–Nb–W–Sn–Zr–Hf mineralization. In: Linnen, R.L., Samson, I.M. (Eds.), Rare-Element Geochemistry and Mineral Deposits. Geological Association of Canada, GAC, Short Course, pp. 45–67.
Liu, Y.J., Ma, D.S., 1987. Geochemistry of Tungsten. Science Press, Beijing (in Chinese).
Liu, Y.J., Cao, L.M., Li, Z.L., Wang, H.N., Chu, T.Q., Zhang, J.R., 1984. Elements Geochemistry. Geology Publishing House, Beijing (in Chinese).
Liu, G.Z., Li, H.M., Wang, J.S., Zhang, T.M., Song, C.Y., 2007. Mineralized body model of the tungsten and tin ore field in Baiganhu, eastern Kunlun, Xinjiang. Xinjiang Geol. 25, 169–173 (in Chinese with English abstract).
Liu, L., Wang, C., Chen, D.L., Zhang, A.D., Liu, J.G., 2009. Petrology and geochronology of HP–UHP rocks from the South Altyn Tagh, northwestern China. J. Asian Earth Sci. 35, 232–244.
Liu, L., Cao, Y.T., Chen, D.L., Zhang, C.L., Yang, W.Q., Kang, L., Liao, X.Y., 2013. New progresses on the HP–UHP metamorphism in the South Altyn Tagh and the North Qinling. Chin. Sci. Bull. 58, 2113–2123 (in Chinese with English abstract).
Loiselle, M.C., Wones, D.R., 1979. Characteristics and origin of anorogenic granites. Geol. Soc. Am. Bull. 11, 468 (Abstracts with Programs).
Maniar, P.D., Piccoli, P.M., 1989. Tectonic discrimination of granitoids. Geol. Soc. Am. Bull. 101, 635–643.
Mao, J.W., Xie, G.Q., Guo, C.L., Chen, Y.C., 2007. Large-scale tungsten–tin mineralization in the Nanling region, South China: metallogenic ages and corresponding geodynamic processes. Acta Petrol. Sin. 23, 2329–2338 (in Chinese with English abstract).
Maulana, A., Watanabe, K., Imai, A., Yonezu, K., 2013. Origin of magnetite- and ilmenite-series granitic rocks in Sulawesi. , Indonesia: Magma genesis and regional metallogenic constraint. Procedia Earth Planet. Sci. 6, pp. 50–57.
Mo, X.X., Luo, Z.H., Deng, J.F., Yu, X.H., Liu, C.D., Chen, H.W., Yuan, W.M., Liu, Y.H., 2007. Granitoids and crustal growth in the East–Kunlun Orogenic Belt. Geol. J. China Univ. 13, 403–414 (in Chinese with English abstract).
Mücke, A., 2003. Fayalite, pyroxene, amphibole, annite and their decay products in mafic clots within Younger Granites of Nigeria: petrography, mineral chemistry and genetic implications. J. Afr. Earth Sci. 36, 55–71.
Neiva, A.M.R., 2002. Portuguese granites associated with Sn-W and Au mineralizations. Bull. Geol. Soc. Finl. 74, 79–101.
Obaje, N.G., 2009. Geology and Mineral Resources of Nigeria. Springer, Berlin, pp. 31–48.
Ogunleye, P.O., Ike, E.C., Garba, I., 2005. Geochemical characteristics of the niobium-rich arfvedsonite granites, Younger Granites province of Nigeria. Chem. Erde 65, 279–296.
Pearce, J.A., Van der Laan, S.R., Arculus, R.J., Murton, B.J., Ishii, T., Peate, D.W., 1992. Boninite and Harzburgite from Leg 125 (Bonin–Mariana Fore-arc): a case study of magma genesis during the initial stage of subduction. In: Fryer, P., Pearce, J.A., Stokking, L.B. (Eds.), Proceedings for the Ocean Drilling Program. Sci. Results 125, pp. 623–659.
Pirajno, F., 2009. Hydrothermal Processes and Mineral Systems. Springer, Berlin.
Polat, A., Hofmann, A.W., Rosing, M.T., 2002. Boninite-like volcanic rocks in the 3.7–3.8 Ga Isua greenstone belt, West Greenland: geochemical evidence for intra-oceanic subduction zone processes in the early Earth. Chem. Geol. 184, 231–254.
Pollard, P.J., Pichavant, M., Charoy, B., 1987. Contrasting evolution of fluorine-and boron-rich tin systems. Mineral. Deposita 22, 315–321.
Pollard, P.J., Taylor, R.G., Cuff, C., 1988. Genetic modelling of greisen-style tin systems. In: Hutchison, C.S. (Ed.), Geology of Tin Deposits in Asia and the Pacific. Springer, Berlin, pp. 59–72.
Rollinson, H.R., 1993. Using Geochemical Data: Evaluation, Presentation, Interpretation. Pearson Education, London.
Rudnick, R.L., Gao, S., 2014. Composition of the Continental Crust. In: Turekian, H.D.H.K. (Ed.), The Crust, second ed. Treatise on Geochemistry vol. 4. Elsevier, Oxford, pp. 1–805.
Ruiz, C., Fernández-Leyva, C., Locutura, J., 2008. Geochemistry, geochronology and mineralisation potential of the granites in the Central Iberian Zone: the Jalama batholith. Chem. Erde-Geochem. 68, 413–429.
Shedd, K.B., 2015. Tungsten (advance release). 2012: U.S. Geological Survey Minerals Year Book, pp. 79.0–79.20.
Skjerlie, K.P., Johnston, A.D., 1996. Vapour–absent melting from 10 to 20 kbar of crustal rocks that contain multiple hydrous phases: implications for anatexis in the deep to very deep continental crust and active continental margins. J. Petrol. 37, 661–691.
Steiger, R.H., Jager, E., 1977. Subcommission on geochronology: convention on the use of decay constants in geo- and cosmochronology. Earth Planet. Sci. Lett. 36, 359–362.
Sun, S.S., McDonough, W.F., 1989. Chemical and isotopic systematic of oceanic basalts: implications for mantle composition and processes. In: Saunders, A.D., Norry, M.J. (Eds.), Magmatism in the Ocean Basins. Geol. Soc. Spec. Publ 42, pp. 313–345.
Sun, F.Y., Li, B.L., Ding, Q.F., Zhao, J.W., Pan, T., Yu, X.F., Wang, L., Chen, G.J., Yu, Z.J., 2009. Study on the major prospecting problem in East Kunlun Metallogeny Belt. Geological Survey Research Institute of Jilin University, Jilin (unpublished data).
Sylvester, P.J., 1998. Post-collisional strongly peraluminous granites. Lithos 45, 29–44.
Taylor, S.R., McLennan, S.M., 1995. The geochemical evolution of the continental crust. Rev. Geophys. 33, 241–265.
Wade, J., Wood, B.J., Norris, C.A., 2013. The oxidation state of tungsten in silicate at high pressures and temperatures. Chem. Geol. 335, 189–193.
Wang, R.C., Wang, D.Z., Zhao, G.T., Lu, J.J., Chen, X.M., Xu, S.J., 2001. Accessory mineral record of magma–fluid interaction in the Laoshan I- and A-type granitic complex, eastern China. Phys. Chem. Earth 26, 835–849.
Wang, C., Liu, L., Luo, J.H., Che, Z.C., Teng, Z.H., Cao, X.D., Zhang, J.Y., 2007. Late Paleozoic post-collisional magmatism in the Southwestern Tianshan orogenic belt, take the Baleigong pluton in the Kokshal region as an example. Acta Petrol. Sin. 23, 1830–1840 (in Chinese with English abstract).
Wang, C., Liu, L., Zhang, A.D., Yang, W.Q., Cao, Y.T., 2008. Geochemistry and petrography of Early Paleozoic Yusupuleke Tagh rapakivi-textured granite complex, South Altyn—an example for magma mixing. Acta Petrol. Sin. 24, 2809–2819 (in Chinese with English abstract).
Wang, W., Liu, S., Feng, Y., Li, Q., Wu, F., Wang, Z., Yang, P., 2012. Chronology, petrogenesis and tectonic setting of the Neoproterozoic Tongchang dioritic pluton at the northwestern margin of the Yangtze Block: constraints from geochemistry and zircon U–Pb–Hf isotopic systematics. Gondwana Res. 22, 699–716.
Wang, C., Liu, L., Xiao, P.X., Cao, Y.T., Yu, H.Y., Joseph, G.M., Liang, W.T., 2014a. Geochemical and geochronologic constraints for Paleozoic magmatism related to the orogenic collapse in the Qimantagh–South Altyn region, northwestern China. Lithos 202–203, 1–20.
Wang, Z.Z., Han, B.F., Feng, C.Y., Li, G.C., 2014b. Geochronology, geochemistry and tectonic significance of granites in Baiganhu area, Xinjiang. Acta Petrol. Mineral. 33, 597–616 (in Chinese with English abstract).
Watson, E.B., Harrison, T.M., 1983. Zircon saturation revisited: temperature and composition effects in a variety of crustal magma types. Earth Planet. Sci. Lett. 64, 295–304.
Whalen, J.B., Currie, K.L., Chappell, B.W., 1987. A-type granites: geochemical characteristics, discrimination and petrogenesis. Contrib. Mineral. Petrol. 95, 407–419.
White, A.J.R., Chappell, B.W., 1977. Ultrametamorphism and granitoid genesis. Tectonophysics 43, 7–22.
Wu, F., Sun, D., Li, H., Jahn, B., Wilde, S., 2002. A-type granites in northeastern China: age and geochemical constraints on their petrogenesis. Chem. Geol. 187, 143–173.
Xu, Z.Q., Yang, J.S., Li, H.B., Yao, J.X., 2006. The Early Paleozoic terrane framework and the formation of the high-pressure (HP) and ultra-high pressure (UHP) metamorphic belts at the Central Orogenic Belt (COB). Acta Geol. Sin. 80, 1793–1806 (in Chinese with English abstract).
Yan, M.C., Chi, Q.H., 1997. The Crust and its Composition of the Eastern China. Science Press, Beijing (in Chinese).
Yang, J.H., Peng, J.T., Hu, R.Z., Bi, X.W., Zhao, J.H., Fu, Y.Z., Shen, N.P., 2013. Garnet geochemistry of tungsten-mineralized Xihuashan granites in South China. Lithos 177, 79–90.
Zhang, Z.Y., Hou, Z.Q., Peng, H.M., Zhu, X.Q., Pan, X.F., Ye, Z.Y., 2015. Exsolution of primary fluids from magma in the superlarge Dahutang tungsten deposit of Jiangxi Province: records from the pegmatoid shell. Geol. Bull. China 34, 487–500 (in Chinese with English abstract).
Zhou, J.H., Feng, C.Y., Zhao, Y.M., Li, D.X., Wang, H., Zhang, M.Y., 2015. Spatial–temporal distribution, mineral deposit geology and prospecting potential of major Paleozoic tungsten–tin deposits in China. China Tungsten Ind. 30, 24–32 (in Chinese with English abstract).